Global monthly water stress: 1. Water balance and water availability

L. P. H. van Beek,[1] Yoshihide Wada,[1] and Marc F. P. Bierkens[1,2]

Received 23 July 2010; revised 14 April 2011; accepted 11 May 2011; published 12 July 2011.

[1] Surface fresh water (i.e., blue water) is a vital and indispensable resource for human water use in the agricultural, industrial, and domestic sectors. In this paper, global water availability is calculated by forcing the global hydrological model PCR-GLOBWB with daily global meteorological fields for the period 1958–2001. To represent blue water availability, a prognostic reservoir operation scheme was included in order to produce monthly time series of global river discharge modulated by reservoir operations. To specify green water availability for irrigated areas, actual transpiration from the model was used. Thus, the computed water availability reflects the climatic variability over 1958–2001 and is contrasted against the monthly water demand using the year 2000 as a benchmark in the companion paper. As the water that is withdrawn to meet demand directly interferes with blue water availability along the drainage network, this paper evaluates model performance for three regimes reflecting different degrees of human interference: natural discharge, discharge regulated by reservoirs, and modified discharge. In the case of modified discharge, the net blue water demand for the year 2000 is subtracted directly from the regulated discharge, taking water demand equal to consumptive water use. Results show that model simulations of monthly river discharge compare well with observations from most of the large rivers. Exceptions are basins subject to large extractions for irrigation purposes, where simulated discharge exceeds the observations even when water demand is taken into account. Including the prognostic reservoir operation scheme results in mixed performance, with a poorer approximation of peak flows but with a marginally better simulation of low flows and persistence. A comparison of simulated actual evapotranspiration with that from the ERA-40 reanalysis as a proxy for observed rates shows similar patterns over nonirrigated areas but substantial deviations over major irrigated areas. As expected, assimilated actual evapotranspiration over these areas includes water from alternative sources, whereas the simulations with PCR-GLOBWB are limited by soil moisture, i.e., green water availability. On the basis of this evidence we conclude that the simulation provides adequate fields of water availability to assess water stress at the monthly scale, for which a separate validation is provided in the companion paper.

Citation: van Beek, L. P. H., Y. Wada, and M. F. P. Bierkens (2011), Global monthly water stress: 1. Water balance and water availability, *Water Resour. Res.*, *47*, W07517, doi:10.1029/2010WR009791.

1. Introduction

[2] The existing imbalance of water availability and water demand causes water scarcity to be one of the most pressing environmental issues in the world today. Water demand is defined here as the volume of water required by users to satisfy their needs. Surface fresh water is the most readily available resource to meet the water demand of agriculture (i.e., irrigation and livestock), industry, households and municipalities. We take surface fresh water as indicative of blue water availability and thus depart from its common definition [e.g., *Falkenmark*, 1997] that includes groundwater resources as well. Rather, we choose to include groundwater as a particular resource in order to identify regions that may experience dwindling availability in the future [*Wada et al.*, 2011]. Despite the fact that the world population currently uses only 10% of the maximum available blue water in the form of river discharge on the global scale [*Oki and Kanae*, 2006], water stress occurs since water availability is highly variable over space and time [*Postel et al.*, 1996]. *Meigh et al.* [1999] noted that water scarcity often first becomes apparent as occasional deficits during periods of high demand or below-average rainfall and may affect a narrow region only. As water availability and demand vary over time, water stress may be underestimated by annual assessments as availability and demand may be out of phase. Therefore, the objective of this study is to quantify at a monthly time scale the seasonal and interannual variations in blue water stress on the global scale when water demand is confronted with climate-induced

[1]Department of Physical Geography, Utrecht University, Utrecht, Netherlands.
[2]Unit Soil and Groundwater Systems, Deltares, Utrecht, Netherlands.

0043-1397/11/2010WR009791

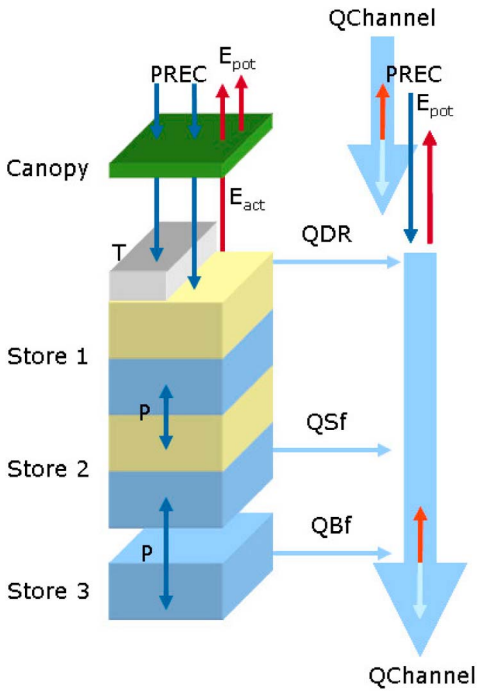

Figure 1. Model concept of PCR-GLOBWB [*van Beek and Bierkens*, 2009]. The left-hand side represents the vertical structure for the soil hydrology representing the canopy, soil column (stores 1 and 2), and the groundwater reservoir (store 3). Precipitation (PREC) falls as rain if air temperature (T) is above 0°C and as snow otherwise. Snow accumulates on the surface, and melt is temperature controlled. Potential evapotranspiration (E_{pot}) is broken down into canopy transpiration and bare soil evaporation, which are reduced to an actual rate (E_{act}) on the basis of the moisture content of the soil. Vertical transport in the soil column arises from percolation or capillary rise (P). Drainage from the soil column to the river network occurs via direct runoff, interflow or subsurface stormflow, and base flow (QDR, QSf, and QBf, respectively). Drainage accumulates as discharge (QChannel) along the drainage network and is subject to a direct gain or loss depending on the precipitation and potential evaporation acting on the freshwater surface (section 2.2).

variability in water availability. This may highlight problem regions that are not represented by existing assessments based on annual totals as well as define the temporal characteristics of water stress for problem regions previously identified.

[3] For our assessment of blue water availability, we make use of the macroscale hydrological model PCR-GLOBWB [*van Beek and Bierkens*, 2009]. The model was run with a spatial resolution of 0.5° and forced with daily meteorological input obtained by downscaling the CRU TS 2.1 monthly data set [*Mitchell and Jones*, 2005] with the ERA-40 reanalysis [*Kållberg et al.*, 2005], giving a common period of 44 years between 1958 and 2001 inclusive. From this model we derived river discharge with inclusion of a prospective reservoir operation scheme similar to that of *Haddeland et al.* [2006] to quantify blue water availability. The results of PCR-GLOBWB are also used to include the effect of available soil moisture on irrigation blue water demand, by taking the simulated actual evapotranspiration under nonirrigation conditions as green water availability [e.g., *Rockström et al.*, 2007, see section 2.2]. Monthly blue water availability is then contrasted against monthly water demand for agricultural, industrial and domestic sector to compute water stress at a global scale. Water demand is defined here as the volume of water required by users to satisfy their needs and that is permanently lost from the available blue water resources (i.e., net demand).

[4] The methodologies and the results of this study are presented in two companion papers. This first paper describes the global hydrological model PCR-GLOBWB and the prospective reservoir scheme used to estimate green and blue water availability at a monthly time scale. Blue water availability is evaluated for three regimes reflecting different degrees of human interference: natural discharge, regulated discharge, where discharge is altered by reservoir operations, and modified discharge, the latter being regulated discharge decreased by the water demand for the benchmark year 2000 as presented in the companion paper by *Wada et al.* [2011]. To gain confidence in the estimated green and blue water availability, simulated river discharge of the larger rivers is compared to observations [*Global Runoff Data Centre* (*GRDC*), 2008], and the calculated evapotranspiration is compared to that of the ERA-40 reanalysis as proxy for observed rates [*Kållberg et al.*, 2005]. The second paper focuses on the calculation of blue water demand and ensuing water stress and its validation against reported water stress on the regional scale, and evaluates the difference between the analyses of water stress made on a monthly and annual time scale.

2. Methods

2.1. PCR-GLOBWB

[5] Water availability was calculated by means of the macroscale hydrological model PCR-GLOBWB [see *van Beek and Bierkens*, 2009]. A schematic representation of the model is given in Figure 1. In essence, it is a "leaky bucket" type of model that is applied on a cell-by-cell basis (0.5° × 0.5° grid globally). PCR-GLOBWB calculates for every grid cell and for every time step the water storage in two vertically stacked soil layers, with maximum depths of 0.3 and 1.2 m, respectively, and for an underlying groundwater reservoir. Changes in storage arise because of the exchange of water between these layers (percolation, capillary rise), depletion (interflow and base flow), and the atmosphere (rainfall, snowmelt and evapotranspiration).

[6] Climatic forcing is applied with a daily resolution and assumed to be constant over the grid cell. Precipitation falls either as snow or rain depending on air temperature. Snow accumulation and melt are temperature driven and modeled according to the snow module of the HBV model [*Bergström*, 1995]. Precipitation can be intercepted by the canopy with limited storage capacity and any intercepted water is subject to open water evaporation. Excess precipitation is added to the snowpack if the air temperature is less than 0°C. Above 0°C precipitation and meltwater are stored as liquid water in the available pore space in the snow cover, or passed on to the first soil layer. Precipitation and air temperature were prescribed by the CRU TS 2.1 monthly data set [*Mitchell and Jones*, 2005], which has

the advantage that it is based on observations, covers the global landmass with the exception of Antarctica, and has been processed in a consistent manner at a grid resolution of 0.5°.

[7] Using the Penman-Monteith equation according to FAO guidelines [*Allen et al.*, 1998], monthly reference potential evapotranspiration, ET_0, is calculated from the secondary variables specified in the CRU TS 2.1 data set and imposed on the model. Monthly values of precipitation, temperature and reference potential evapotranspiration are subsequently broken down to daily values using the ECMWF ERA-40 reanalysis [*Kållberg et al.*, 2005]. This limits the climate series to the calendar years of 1958 to 2001 for which ERA-40 data are available. Multiplicative anomalies are applied to the daily ERA-40 precipitation, additive anomalies to the daily ERA-40 2m air temperature while monthly reference potential evapotranspiration is disaggregated on the basis of the normalized daily temperature [*van Beek*, 2008]. A similar approach was followed for the spin-up of the model in which the CRU climatology was used to represent average meteorological conditions and downscaled with daily ERA-40 fields that equally represent the long-term mean. Simulation with this forcing was repeated until a dynamic steady state was achieved from which the initial model states were retrieved.

[8] Subgrid variability is taken into account by considering separately tall and short vegetation, open water and different soil types. Direct runoff is generated by liquid precipitation falling on fully saturated soil, which fraction is based on the improved ARNO scheme of *Hagemann and Gates* [2003]. This scheme is parameterized on the subgrid distribution of rooting depths and the variation in elevation within each cell. The total specific runoff in a cell consists of the direct runoff and lateral drainage from the soil profile (interflow) and the groundwater reservoir (base flow). Interflow is modeled by a simplified approach based on the work of *Sloan and Moore* [1984] and *Ormsbee and Khan* [1989] in which the soil is idealized as a uniform, sloping slab with an average soil depth and inclination. Base flow is modeled by a linear reservoir for which the response time is parameterized on the basis of a global map of lithology [*Dürr et al.*, 2005] and drainage density derived from the Hydro1k data set [*Verdin and Greenlee*, 1996] (Land Processes Distributed Active Archive Center, HYDRO1k Elevation Derivative Database, http://eros.usgs.gov/#/Find_Data/Products_and_Data_Available/gtopo30/hydro). River discharge is accumulated and routed along the drainage network using kinematic wave routing with a time-explicit scheme and variable time stepping and includes evaporative losses from lakes, reservoirs and floodplains.

2.2. Green Water: Potential and Actual Transpiration

[9] Soil moisture that is available to plants, including crops, or so-called green water is replenished by infiltration and capillary rise. When calculating blue water irrigation demand, green water availability needs to be taken into account. Blue water irrigation demand is based on the difference between potential transpiration and actual transpiration under nonirrigated conditions. The crop- and plant-specific transpiration in PCR-GLOBWB is calculated according to the FAO guidelines [*Allen et al.*, 1998]. In brief (see *van Beek* [2008] and *Wada et al.* [2011] for details), the crop- and plant-specific potential evapotranspiration, ET_c (m d^{-1}), is calculated from

$$ET_c = k_c ET_0, \tag{1}$$

where ET_0 is the reference potential evapotranspiration (m d^{-1}), and k_c is a crop factor (dimensionless). Following FAO guidelines for monthly crop water requirements, reference potential evapotranspiration is calculated with the Penman-Monteith equation [*Monteith*, 1965] for a hypothetical grass surface with a specified height of 0.12 m, an albedo of 0.23 and a surface resistance of 70 s m^{-1} [*Allen et al.*, 1998]. For the meteorological data, the monthly data of cloud cover, vapor pressure, and average air temperature from the CRU TS 2.1 data set are used. For wind speed, which is absent in the time series, the monthly climatology over the years 1961–1990 from the earlier CRU CLIM 1.0 data set are used [*New et al.*, 1999]. Monthly extraterrestrial radiation is calculated separately on the basis of Julian day number and latitude in order to estimate the net incoming short-wave radiation and outgoing long-wave radiation using the empirical relationships of *Doorenbos and Pruitt* [1977] and *Allen et al.* [1998].

[10] The crop factor combines the effect of individual plants and stands on the potential crop transpiration and bare soil evaporation. Although originally developed for real crops, the approach can be expanded to natural vegetation [*Allen et al.*, 1998]. Conform to the land surface parameterization in PCR-GLOBWB, the crop factors are specified on a monthly basis for the short and tall vegetation fractions, as well as for the open water fraction within each cell. For the vegetated surfaces, the GLCC version 2 at 30 arc seconds (Earth Resources Observation and Science Center, U.S. Geological Survey, Global land cover characteristics data base version 2.0, http://edc2.usgs.gov/glcc/glcc.php) land cover types [*Olson*, 1994a, 1994b] were divided into three categories: natural vegetation, rain-fed crops and irrigated crops, each category being broken down into short and tall vegetation. For all these crop types, leaf area index (LAI) values at dormancy and at the peak of their growing season were obtained from *Hagemann et al.* [1999]. These values were linked to a climatology of relative LAI at 0.5° that was based on the monthly CRU climatology of temperature, precipitation and potential evapotranspiration over 1961–1990, thus returning the length of the growing season on the basis of temperature and moisture availability criteria [*van Beek*, 2008]. It was assumed that vegetation will use the available growing season fully either through natural competition or human intervention (e.g., multiple cropping systems, foraging and green fertilization, etc.). The returned LAI climatology for every GLCC land cover type was converted into a monthly crop factor by using the following relationship [*Allen et al.*, 1998]:

$$k_c = k_{c\min} + \left(k_{cfull} - k_{c\min}\right)[1 - \exp(-0.7\mathrm{LAI})], \tag{2}$$

where $k_{c\ \min}$ is the minimum crop factor for bare soil (0.20), $k_{c\ full}$ is the estimated crop factor under full cover conditions and LAI is the monthly LAI for the specific land cover type (m^2 m^{-2}). The crop factor under full cover conditions is a function of the vegetation height and ranges between 1 and 1.2 (dimensionless) and corrected for meteorological conditions that differ from the reference conditions in relative

humidity and wind speed [*Allen et al.*, 1998]. As the scaling of the reference potential evapotranspiration to the crop-specific value is linear, the resulting monthly crop factors at 30 arc seconds were averaged to 0.5° effective values for the short and tall vegetation fractions for the respective categories of natural vegetation and rain-fed and irrigated crops.

[11] The monthly potential evapotranspiration for the short and tall vegetation is broken down into daily values on the basis of daily ERA-40 2m air temperature, normalized by the monthly averaged value. Since ET_c describes the potential evapotranspiration, it is converted into potential bare soil evaporation, ES_0, and potential transpiration, T_c (both in m d^{-1}) by

$$ES_0 = k_{c\min} ET_0, \tag{3}$$

$$T_c = ET_c - ES_0 = k_c ET_0 - k_{c\min} ET_0 = (k_c - k_{c\min}) ET_0, \tag{4}$$

Before the potential bare soil evaporation and transpiration are passed to the soil, they may evaporate any free liquid water that is stored in the snow cover or on the canopy, respectively. Evaporation and transpiration losses from the soil will be reduced as the matric potential resists extraction from unsaturated soil. Bare soil evaporation is drawn from the topsoil only and no reduction is applicable, except that the potential evaporation rate cannot exceed the saturated hydraulic conductivity of the topsoil for the saturated fraction, x, within each cell as obtained by the Improved ARNO Scheme of *Hagemann and Gates* [2003]. Likewise, for the unsaturated fraction, the rate is restricted by the unsaturated hydraulic conductivity, $k(\theta_{E1})$ (m d^{-1}), of the upper soil layer:

$$ES = x \min(k_s, ES_0) + (1 - x) \min[k(\theta_{E1}), ES_0], \tag{5}$$

where θ_{E1} is the effective degree of saturation in layer 1 (m m^{-1}).

[12] The lack of aeration prevents the uptake of water by roots under fully saturated conditions and transpiration only takes place over the unsaturated fraction 1-x of the cell. Over this area, actual transpiration depends on the total available soil moisture in the soil layers. Potential transpiration is thus reduced to actual transpiration, T_a (m d^{-1}):

$$T_a = (1 - x) f_T T_c, \tag{6}$$

with f_T, the actual to potential transpiration rate given by

$$f_T = \frac{1}{1 + (\theta_E / \theta_{E50})^{-3\beta}}, \tag{7}$$

where θ_{E50} is the average degree of saturation at which the potential transpiration is halved, taken to be equivalent to a degree of saturation associated with a matric suction of 33.3 kPa, and β is the coefficient of the *Clapp and Hornberger* [1978] soil water retention curve.

[13] The parameters of equation (7) are calculated from the properties of the two soil layers, weighed by their soil water storage capacity and root fractions. Expanding on the Improved Arno Scheme, the average degree of saturation, θ_E, over the unsaturated fraction of the cell is [*van Beek*, 2008]:

$$\theta_E = \frac{W_{\max} + b(W_{\max} - W_{\min}) \left[1 - \frac{b+1}{b} \left(\frac{W_{\max} - W}{W_{\max} - W_{\min}} \right)^{\frac{1}{b+1}} \right]}{W_{\max} + b(W_{\max} - W_{\min}) \left[1 - \left(\frac{W_{\max} - W}{W_{\max} - W_{\min}} \right)^{\frac{1}{b+1}} \right]}, \tag{8}$$

where W, $W_{\max}$, and $W_{\min}$ are the cell-averaged total soil moisture storage and maximum and minimum storage capacities, respectively (all in m), and b is the shape factor (dimensionless) describing the distribution of the local soil moisture storage capacity, w.

[14] Transpiration can be drawn from both soil layers, with the actual transpiration rate being partitioned by

$$T_{ai} = T_a \frac{r_i \theta_{Ei}}{\sum r_i \theta_{Ei}}, \tag{9}$$

where r is the root fraction (dimensionless) and θ_{Ei} is the effective degree of saturation for layer i.

[15] The simulated actual transpiration specifies the amount of water that vegetation can withdraw from the soil for assimilation under natural conditions. Over irrigated areas, it covers that part of the transpiration that is supplied by green water and is used as such to obtain the blue water irrigation demand as outlined in the companion paper [*Wada et al.*, 2011].

2.3. River Discharge and Blue Water Availability

[16] Blue water availability is taken equal to the renewable surface freshwater volume, i.e., river discharge. In PCR-GLOBWB, river discharge is the result of the local specific runoff over the land surface and the direct gains or losses due to precipitation and evaporation over the open water surface. The specific discharge of each cell is routed over a drainage network that defines flow in eight cardinal directions (NW, N, NE, E, SE, S, SW, and W). This drainage network either terminates at the ocean or at an inland sink in the case of land-locked basins. Essential to the routing scheme is that the drainage network is subdivided into river stretches and lake areas, including reservoirs that can be treated separately. Open water evaporation occurs at the potential rate, with different monthly crop factors being applied to deep water (lakes and reservoirs) and shallow water (river stretches) as suggested by *Allen et al.* [1998].

[17] For the river stretches, which include both channels and associated floodplains, discharge is calculated by the kinematic wave approximation of the Saint-Venant equation [*Chow et al.*, 1988]. This entails that at the end of each time step, a new stage for the simulated discharge is calculated under an assumption of a rectangular channel and passed on to the next time step to estimate the wetted perimeter of the flow and the corresponding roughness from the Manning equation [*Dingman*, 1994]. In this procedure, floodplains and channels proper are blended into a single, larger channel with a constant width and Manning's roughness coefficient.

[18] Lake areas, including reservoirs, are treated as contiguous water surfaces of fixed extent with a variable water height that changes instantaneously with the net inflow over that area. The net inflow is the balance of inflow and outflow if the lake interrupts the drainage network. The inflow includes the incoming river discharge. For lakes the outflow

Table 1. Objective Functions Used by the Reservoir Model[a]

Purpose	Objective Function[b]
Water supply[c]	$\min \sum_{m=1}^{12} (Q_{dm} - Q_{rm}),\ Q_d > Q_r$
Flood control	$\min \sum_{m=1}^{12} (Q_{rm} - Q_{flood})^2,\ Q_r > Q_{flood}$
Hydropower	$\min \sum_{m=1}^{12} \frac{1}{P_m \cdot Q_{rm} \cdot \rho \cdot g \cdot h_m}$
Navigation	$\min \sum_{m=1}^{12} (Q_{rm} - \overline{Q})$

[a]After *Haddeland et al.* [2006] and *Adam et al.* [2007].

[b]Q_d, forecasted water demand; Q_r, reservoir release; Q_{flood}, bankfull discharge; $\overline{Q}$, mean annual discharge; P, variations in the price of hydropower; ρ, density of water; η, efficiency of power generating system; h, hydrostatic pressure head (water height in reservoir with respect to downstream level); g, acceleration due to gravity.

[c]Water supply covers net irrigation water demand (blue water) and gross industrial and domestic water demand.

is calculated in analogy to the weir formula as the discharge over a rectangular cross section [*Bos*, 1989]:

$$Q_{Out} = C\tfrac{2}{3}\sqrt{\tfrac{2}{3}g}\, b(h - h_0)^{3/2}\Delta t \approx 1.70Cb(h - h_0)^{3/2}\Delta t, \quad (10)$$

where b is the breadth of the outlet (m), g is the gravitational acceleration (m s^{-2}) and h and h_0 are the actual lake level and the sill of the outlet (m), respectively. C is a factor (m$^{4/3}$ s^{-1}) that corrects among others for the effects of back and tail waters, viscosity, turbulence and deviations from the assumed uniform flow distribution, which was kept at unity in this study.

[19] The discharge at the outlet of lakes and reservoirs (see below) is added within the time step to the lateral inflow in the kinematic wave approximation of the downstream river stretches. The resulting daily discharge along the drainage network was then averaged to mean monthly values to obtain the blue water availability.

[20] The routing scheme in PCR-GLOBWB is parameterized from different sources. Channel dimensions were obtained from allometric relationships between channel width and depth and bankfull discharge, which were extrapolated over the globe using a statistical relationship derived from 296 stations taken from the RivDis data set [*Vörösmarty et al.*, 1998]. Floodplain extent was defined as the minimum of the area as specified by the GLWD3 data set [*Lehner and Döll*, 2004] and the area flooded by water levels 1 m above the stage at bankfull discharge for the DEM of the Hydro1k data set [*Verdin and Greenlee*, 1996]. A selection of substantial lakes (≥500 km^2), and reservoirs (see below), was taken from the GLWD1 data set [*Lehner and Döll*, 2004], corresponding to 85% of the surface areas of the lakes specified. This selection was replenished with smaller lakes, taken from the GLWD3 data set, to provide evaporative surfaces at the sinks of land-locked basins.

2.4. Inclusion of Reservoirs

[21] Most of the world's major rivers are regulated by artificial reservoirs [*Vörösmarty et al.*, 2004; *Nilsson et al.*, 2005] with the purpose to retain above-average discharge such as spring floodwaters stemming from snowmelt for later use [*Jackson et al.*, 2001] or controlled release. Since the total storage capacity of reservoirs (7000 km^3 globally) comprises three times the annual average water storage in river channels (1200–2120 km^3) and one sixth of the global annual river discharge (40,000 km^3 yr^{-1} [*Baumgartner and Reichel*, 1975]), the effect of reservoir operations on river discharge is not negligible. To account for this effect, different schemes simulating the effect of reservoir operations exist [e.g., *Dynesius and Nilsson*, 1994; *Vörösmarty et al.*, 1997; *Meigh et al.*, 1999; *Coe*, 2000; *Nilsson et al.*, 2005; *Haddeland et al.*, 2006; *Hanasaki et al.*, 2006]. To evaluate the regulating effects of reservoir operations on blue water availability we included a reservoir operation scheme that is similar in nature to that of *Haddeland et al.* [2006]. The main difference is that our scheme is prospective in contrast to the existing schemes of *Haddeland et al.* [2006] and *Hanasaki et al.* [2006] that involve a retrospective regulation on the basis of the simulated discharge and demand. Whereas such retrospective regulation will ensure optimum reservoir performance given its purpose and the given values of inflow and demand, a prospective scheme has to work with uncertain forecasts of future inputs and demands, a reality that confronts reservoir operators on a daily basis. This prospective reservoir operation scheme is directly implemented in the routing model and does not require a priori knowledge of future discharge. As such, both gradual changes in the long-term expectancies of demand and inflow as well as short-term variations thereof can be evaluated continuously over the full extent of a basin and used to update reservoir operations efficiently.

[22] The overall modeling strategy of the prospective reservoir operation scheme of PCR-GLOBWB is to determine the target storage over a defined period ensuring its proper functioning given the forecasts of inflow and downstream demand. Target storage rather than outflow is used as operations have to be updated when actual inflow and demand start to differ from their forecasted values. Updates are carried through at the daily time step on which the routing scheme is run rather than at the monthly scale for which the forecasts in the form of past average values are available. The approach applies to single reservoirs although downstream reservoirs are influenced by the operations at upstream dams. Similar to the work by *Haddeland et al.* [2006], four reservoir types are distinguished, being water supply, including irrigation, flood control, hydropower generation and navigation (Table 1).

[23] Fundamental to the prospective reservoir operation scheme is the concept of the operational year, which starts with the month that the inflow falls below the mean annual value [*Hanasaki et al.*, 2006] and comprises a release period, during which more water is released than what is coming in, and a recharge period, when the situation is reversed. The inflow comprises all incoming discharge, local gains or losses over the reservoir surface and any local freshwater abstractions (currently set to zero). For each month of the coming operational year the expected inflow, $\hat{Q}_{my+1}$, has to be estimated:

$$\hat{Q}_{my+1} = w\overline{Q}_{my-1} + (1 - w)Q_{my}, \quad (11)$$

where Q_{my} is the inflow into the reservoir (m^3 s^{-1}) of the same month of the previous year, $\overline{Q}_{my-1}$ the average inflow

of the particular month averaged over N - 1 retrospective years, $w = 1 - 1/N$, is a weight [0–1] determining the size of the averaging window, and the indices m and y denote the months (1–12) and the elapsed model years, respectively. Currently, the window length of the running average, N, is set to 5 years. In a similar manner, forecasts of downstream water demand are obtained for each reservoir [see *Wada et al.*, 2011] and allocated to the reservoir outlet (see below).

[24] Reservoir operations are optimized on the basis of reservoir release using criteria similar to those of *Haddeland et al.* [2006] (Table 1). Given current reservoir storage and the forecasted inflow and demand, the objective is to find the monthly releases and corresponding reservoir storages that would ensure optimum functioning of the reservoir for a predefined period. For expediency, optimization is invoked twice a year, at the start of the release period and at the start of the recharge period while the long-term expected values of inflow and demand are updated at the end of every month. This means that the timing and the volume of the monthly releases may vary according to changes in the inflow and demand. For every reservoir, optimization involves the evaluation of the criteria of Table 1 and the update of 12 parameters, i.e., the releases for the coming 12 months. In order to reduce the size of the optimization problem, the monthly release is assumed to follow the following harmonic function:

$$Q_{rm} = \frac{Q_{r,\max}}{2} - \frac{Q_{r,\max}}{2}\cos\left(\frac{2\pi(m - m_b)}{(m_e - m_b)}\right), \tag{12}$$

where m_b and m_e are the beginning and the end of the release and recharge period, respectively, and $Q_{r,\max}$ is the maximum release during each period. Thus, twice a year only two parameters need to be optimized, being $Q_{r,\max}$ for the release and recharge period, instead of 12. For the optimization a composite objective function is used. In case a reservoir has multiple purposes, the criteria are weighed proportionally by their rank order [from *International Commission on Large Dams* (*ICOLD*), 2003] with overall precedence being given to water supply. Flood damages are expected if the release exceeds the level of bankfull discharge, Q_{flood}, being 2.3 times the mean annual discharge [*Haddeland et al.*, 2006]. For hydropower generation, we include the option to weigh the objective function by price as proposed by *Adam et al.* [2007], but kept this constant in absence of reliable information. The dependence between reservoir storage, V (m^3), reservoir level, h (m), and surface area, A (m^2), is given by the theoretical relationship of *Liebe et al.* [2005] in which the reservoir volume is represented by a diagonally cut pyramid with a square base, of which the square angle is located at the base of the dam:

$$V = {}^1\!/_3 A d, \tag{13}$$

where d is the reservoir depth or dam height (m), being half the diagonal of the square base, and $A = l^2/2$, where l (m) is the characteristic length. On the basis of a linear dependence between reservoir depth and characteristic length, $d = l/f$, where f is a dimensionless constant [*Liebe et al.*, 2005], the following relation between actual reservoir storage and reservoir level can be defined:

$$h = \sqrt[3]{\frac{6V}{f^2}}. \tag{14}$$

Through equation (13) reservoir storage influences surface area and the associated direct gains and losses by precipitation and evaporation, through equation (14) it determines the reservoir level. The mean monthly reservoir level, used in the objective function for hydropower generation (see Table 1), is given by the harmonic mean of the values at the start and end of the current month. In addition to the criteria of Table 1, there is the practical constraint that the reservoir capacity may never be exceeded and sufficient capacity must be reserved to accommodate excessive discharge. Also, sufficient storage should be kept in reserve to safeguard a certain minimum release. To define these levels, the 7 day maximum $Q_{\max}$ and minimum $Q_{\min}$ discharges were used. The reservoir should hold sufficient water to sustain the release for a month at the rate $Q_{\min}$ and sufficient buffering capacity should be available to store large discharge events that were taken equal to seven times $Q_{\max}$. A 7 day running window is used during the simulation to retrieve the mean discharge and the extremes $Q_{\min}$ and $Q_{\max}$ updated whenever their current value is exceeded. These updated values are then used when reservoir operations are optimized. Similarly, the mean annual discharge, Q_{avg}, is updated on the basis of the running monthly means of equation (11). Initial values for $Q_{\min}$, $Q_{\max}$ and Q_{avg} were obtained from the daily discharge climatology of the spin-up run. During optimization, the overall objective function of the minimization problem is penalized by adding the number of times that any of the above constraints on minimum discharge or flood levels is violated.

[25] Given the prescribed monthly release Q_{rm} of equation (12), the target reservoir storage, S_{m+1} (m^3) becomes

$$S_{m+1} = S_m + n\left\{\left(\hat{Q}_m - Q_{rm}\right)\Delta t + \hat{q}_{wm}A_m\right\} \tag{15}$$

where n is the number of days in the given month, $\hat{Q}_m$ is the expected monthly inflow (equation (11)), $\hat{q}_w$ is the forecasted net gain or loss (m d^{-1}) over the reservoir surface area A, which is the average for the values at times m and $m + 1$.

[26] These monthly target storages are subsequently used to calculate the daily reservoir release. As daily values of inflow become available, actual storage may start to deviate from the originally target storages. However, given the imperfect knowledge for the remainder of the operational year, reservoir operation can still be expected to be optimal during the upcoming months if the final target storage is met. Thus, the daily water releases from a reservoir are modified in an attempt to meet the specified target storage as follows:

$$Q'_{rmi} = \max\left(0, \frac{S_{m,i-1} - S_{m+1}}{(n - i)\Delta t} + \hat{Q}_{mi}\right), \tag{16}$$

where Q'_{rmi} is the updated daily release on the basis of the expected average daily inflow $\hat{Q}_{mi}$ over the remainder of the current month, $S_{m,i-1}$ is the actual storage at the end of

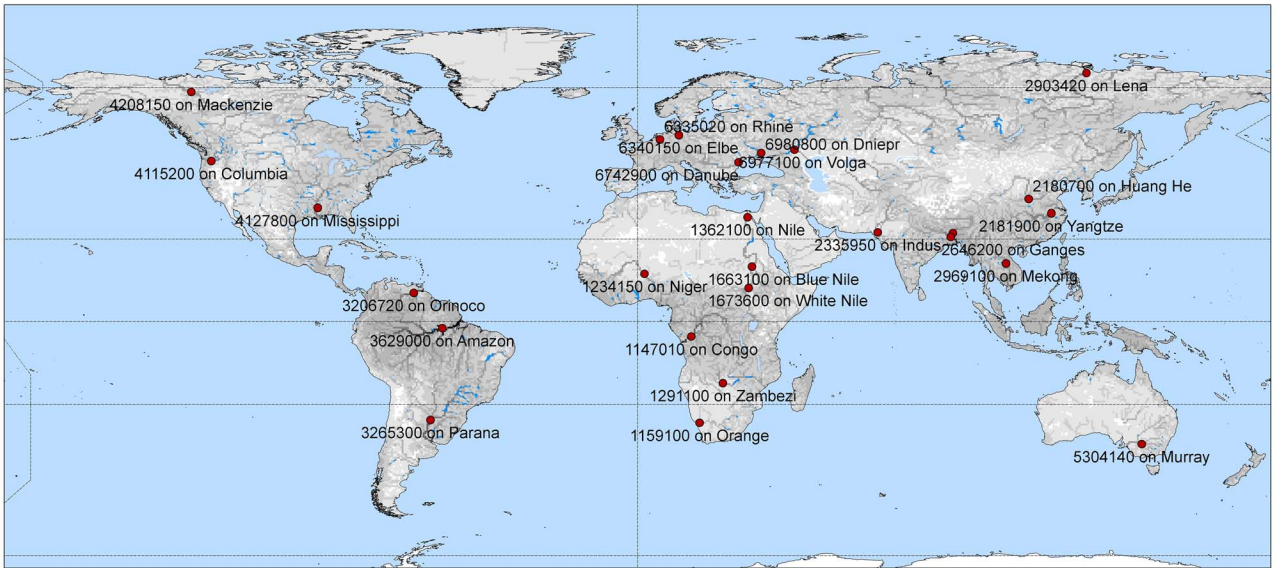

Figure 2. Location of selected Global Runoff Data Centre (GRDC) stations and reservoirs included in the model. Reservoirs are shown by a solid dark blue color, and GRDC stations are shown as circles with the associated GRDC station number and river name (see also Table 2).

the previous day, n is the total number of days for the current month and i is the number of days already passed and Δt is the length of a day in seconds.

[27] Both the expected average daily inflow $\hat{Q}_{mi}$, as well as the expected average daily demand, are updated on the basis of the actual mean value over the elapsed days i and the long-term average for the remainder of the month.

[28] If applicable, the computed daily release Q'_{rmi} of equation (16) is further modified as follows: (1) a reduction in case reservoir storage is below a minimum (10% of reservoir capacity) or in case actual demand to date is below the original monthly forecast; (2) a subsequent increase if actual demand to date is above the original monthly forecast, in the hope to recuperate the additional release at a later time. Obviously, the updated daily reservoir release may not exceed Q_{flood} to ensure downstream safety and the minimum flow $Q_{\min}$ should be met as long as possible. Thus, the daily release from a reservoir responds to short-term variations in the downstream demand and actual inflow, including the release from upstream reservoirs.

[29] Release from a reservoir can only meet the demand in cells that are situated downstream from the reservoir, have an elevation that is less than that of the dam position and that could be reached within 7 days with an average discharge velocity of 1 m s^{-1} (equivalent with 600 km). As an additional constraint, we limited the supply to cells that were located in the same country as the dam. Cells that receive water from multiple reservoirs have their demand weighed by reservoir capacity irrespective whether these reservoirs are located on the same river course or on different tributaries.

[30] Particularly the expansion of irrigated areas has instigated the creation of many new reservoirs [*Avakyan and Ovchinnikova*, 1971; *Haddeland et al.*, 2006; *Biemans et al.*, 2011]. In this assessment the purpose and presence of each dam were kept constant, being representative for the year 2000. Thus, some of the dams are hypothetically present if they are built after 1958 in the subsequent validation of simulated against observed discharge. In total we considered 513 reservoirs (Figure 2) of the 654 reservoirs contained by the GLWD1 data set of *Lehner and Döll* [2004], which incorporates and adds to the information from the WWDR-II and WRD data sets [*Vörösmarty et al.*, 1997; *ICOLD*, 2003] for the world's largest reservoirs (storage capacity ≥0.5 km^3). Of the 513 included reservoirs, 105 (20%) have no year of dam completion listed whereas 247 (48%) are listed as constructed prior to 1970 (GLWD1 [*Lehner and Döll*, 2004]). The GLWD1 data set was preferred as it lists the upstream area for most reservoirs, thus allowing for an accurate positioning of the reservoir on the drainage network. The reservoirs that could not be placed had an upstream area that was smaller than the size of the corresponding cell or fell in a cell that already contained a larger reservoir, in which case they were merged into a single, larger reservoir. The selected reservoirs represent 94% of the area of 255109 km^2 and 95% of the capacity of 4615 km^3 contained by the GLWD data set of *Lehner and Döll* [2004]. This corresponds with 65% of the global total of 7000 km^3 mentioned by *Baumgartner and Reichel* [1975]. The missing reservoirs cannot be truthfully represented given their limited size and catchment area and the required information on their purpose and characteristics is lacking. Thus, their influence on the routing of runoff has been ignored and the findings of this study should be interpreted as a representation of the influence of a limited, if substantial, number of reservoirs on the streamflow. In order to evaluate the effect of the reservoir operation scheme on the simulated discharge, we evaluated the scheme without any reservoirs present (regulated versus natural streamflow) and, as a postprocessing step, with and without abstraction of the net blue water demand (regulated versus modified streamflow). According to the GLWD1 five lakes are regulated (Lake

Table 2. Selected GRDC Stations[a]

Station	Name	River	Latitude	Longitude	Elevation	Q	Area
3629000	Obidos	Amazon	−1.9	−55.5	37	176418	4,640,300
3206720	Puente Angostura	Orinoco	8.2	−63.6	-	31206	836,000
3265300	Corrientes	Parana	−28.0	−58.9	42	16595	2,102,402
1147010	Kinshasa	Congo	−4.3	15.3	-	48903	3,475,000
1362100	El Ekhsase	Nile	29.7	31.3	20	1251	2,900,000
1663100	Khartoum	Blue Nile	15.6	32.6	363	1513	311,870
1673600	Malakal	White Nile	9.6	31.6	389	939	1,084,140
1234150	Niamey	Niger	13.6	2.0	175	887	850,479
1159100	Vioolsdrif	Orange	−28.8	17.6	-	286	850,530
1291100	Katima Mulilo	Zambezi	−17.5	24.3	940	1169	334,000
5304140	Wakool Junction	Murray	−34.8	143.3	-	188	246,015
2969100	Mukdahan	Mekong	16.5	104.7	124	7968	391,000
2651100	Bahadurabad	Brahmaputra	25.2	89.7	19	21112	636,130
2646200	Hardinge Bridge	Ganges	24.1	89.0	14	11157	846,300
2335950	Kotri	Indus	25.4	68.3	13	2904	975,000
2181900	Datong	Yangtze	30.8	117.6	19	28521	1,705,383
2180700	Sanmenxia	Huang He	34.8	111.2	280	1260	688,421
4127800	Vicksburg	Mississippi	32.3	−90.9	14	17150	2,964,255
4115200	The Dalles	Columbia	45.6	−121.2		5371	613,827
4208150	Norman Wells	Mackenzie	65.3	−126.8	50	9476	1,570,000
2903420	Kyusyur	Lena	70.7	127.7	-	16704	2,430,000
6977100	Volgograd Power Plant	Volga	48.8	44.6	-	8141	1,360,000
3980800	Dniepr Power Plant	Dniepr	47.9	35.2	44	1492	463,000
6742900	Ceatal Izmail	Danube	45.2	28.7	1	6415	807,000
6335020	Rees	Rhine	51.8	6.4	8	2253	159,300
6340150	Wittenberge	Elbe	53.0	11.8	17	679	123,532

[a]Latitude and longitude are given in decimal degrees, elevation is in m, average discharge is in $m^3\ s^{-1}$, and area is in km^2 [*GRDC*, 2008].

Victoria, Lake Baikal, Lake Ontario, Lake Reindeer and Lake Nipigon). However, in both situations these lakes are treated as lakes rather than as reservoirs and their outflow being based on equation (10).

3. Results

3.1. Comparison of River Discharge

3.1.1. Data

[31] To acquire confidence in the estimated blue water availability, we compared the river discharge simulated with PCR-GLOBWB with observed values at yearly and monthly time scales using data from the GRDC. Two sets of stations were selected from the GRDC repository, that containing the long-term monthly discharges and annual characteristics [*GRDC*, 2008] and a subset of 26 stations representing the larger basins, which cover a variety of climate zones, latitudes and continents. The data set of long-term stations contains basic statistics, mean, minimum, and maximum discharge, for 3613 GRDC stations with drainage areas larger than 2500 km^2. For the stations of these data set, the observation period may differ from the simulation period and the provided statistics are derived ones only (monthly climatology, annual time series and summary statistics). Moreover, because of the coarse spatial resolution of the model (0.5°), the upstream drainage area of stations, particularly the smaller ones, cannot be represented accurately in all cases. Notwithstanding, this data set provides a good starting point to evaluate the skill of the model to simulate discharge variations within and between years for varying catchment sizes and regions. Selected were those stations with sufficient data (more than 10 years of monthly data), that could be placed on the drainage network of the model with less than 10% error in their drainage area and that did not coincide with lake or reservoir cells other than the outlet, as the reported values here may differ substantially from those of the tributary streams. Of the selected stations, three stations were excluded as the observed values were suspect (being the stations 2998501, 6971450, and 3620100; e.g., the latter, the Rio Ica has a reported mean annual discharge of 46053.2 $m^3\ s^{-1}$ and a drainage area of 108362 km^2, whereas the Congo at Brazzaville has a mean annual discharge of 41116.6 $m^3\ s^{-1}$ and a drainage area of 3614925 km^2). This leaves a total of 2219 stations of which 146 represent the outlet of a lake or reservoir. These stations represent 62% of the 3613 available stations, 84% of the total reported drainage area, and 77% of the reported total discharge. The long-term inventory includes 23 out of the 26 selected stations (Figure 2 and Table 2); those on the Amazon and the Columbia were excluded from the long-term analysis as they were located on lake cells other than the actual outlet.

3.1.2. Data Analysis

[32] Three different regimes were simulated, being natural discharge, regulated discharge and modified discharge, and differences in simulated mean annual discharge explored in Figure 3. As a first comparison, the observed discharges were regressed on the simulated values. To standardize for the effect of drainage area and cancel out any deviations therein, also the catchment-averaged runoff was calculated and regressed (Figure 4). To investigate possible causes for the differences in performance over the large sample of long-term statistics for the GRDC data set, we categorized all catchments by size and observed runoff and evaluated performance in terms of the relative deviation in catchment-averaged runoff, expressed in terms of order of magnitude, the correlation coefficient for the climatology of monthly discharges, and that for the time series of annual discharges (Figures 5, 6, and 7, respectively). The deviations show how well the total runoff is approximated, whereas the latter two

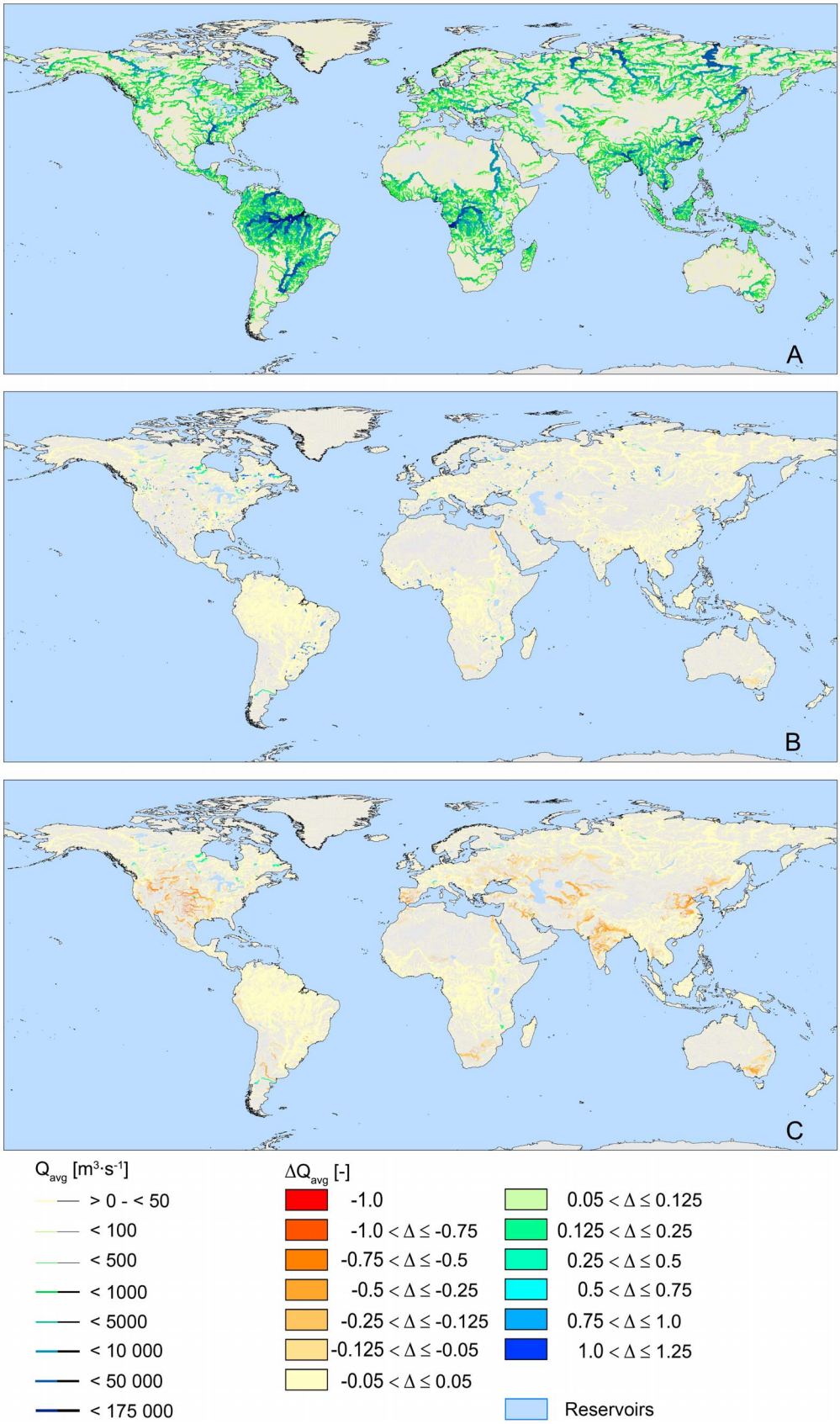

Figure 3. (a) Simulated mean annual natural discharge ($m^3\ s^{-1}$) over the period 1958–2001 and relative change $(\overline{Q} - \overline{Q}_{natural})/\overline{Q}_{natural}$ (dimensionless) in the case of discharge (b) regulated by reservoirs and (c) further modified by water demand. Negative changes denote a decrease in discharge; positive ones indicate an increase.

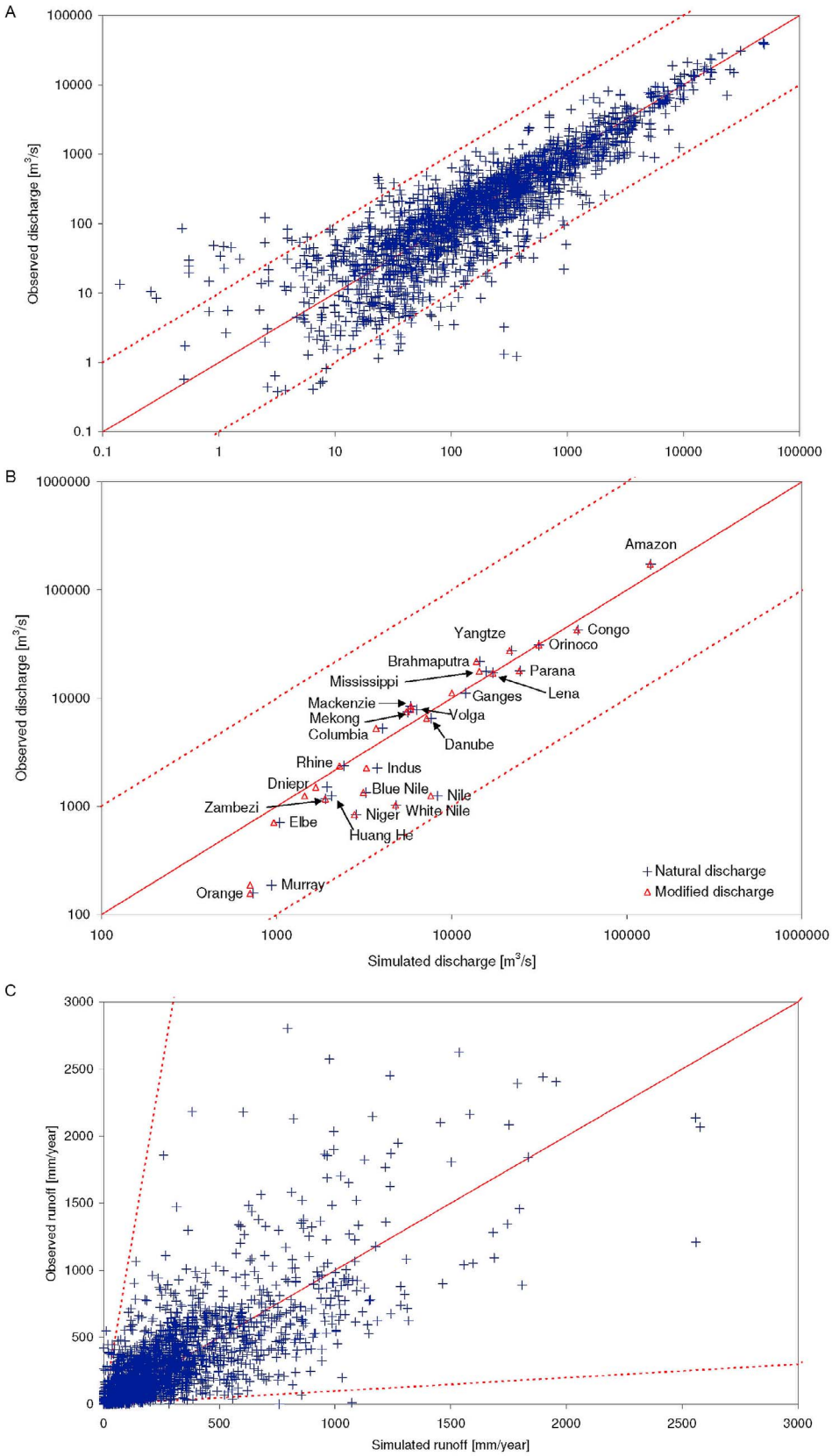

Figure 4. Observations versus simulations of discharge and runoff for the selected GRDC stations: natural discharge (a) for the 2219 stations of the long-term GRDC data set [*GRDC*, 2008] and (b) for the 26 selected large river basins and (c) the same as Figure 4a, but depicting mean annual runoff. The solid line represents the 1:1 slope, and the dashed lines indicate bound values differing by less than one order of magnitude.

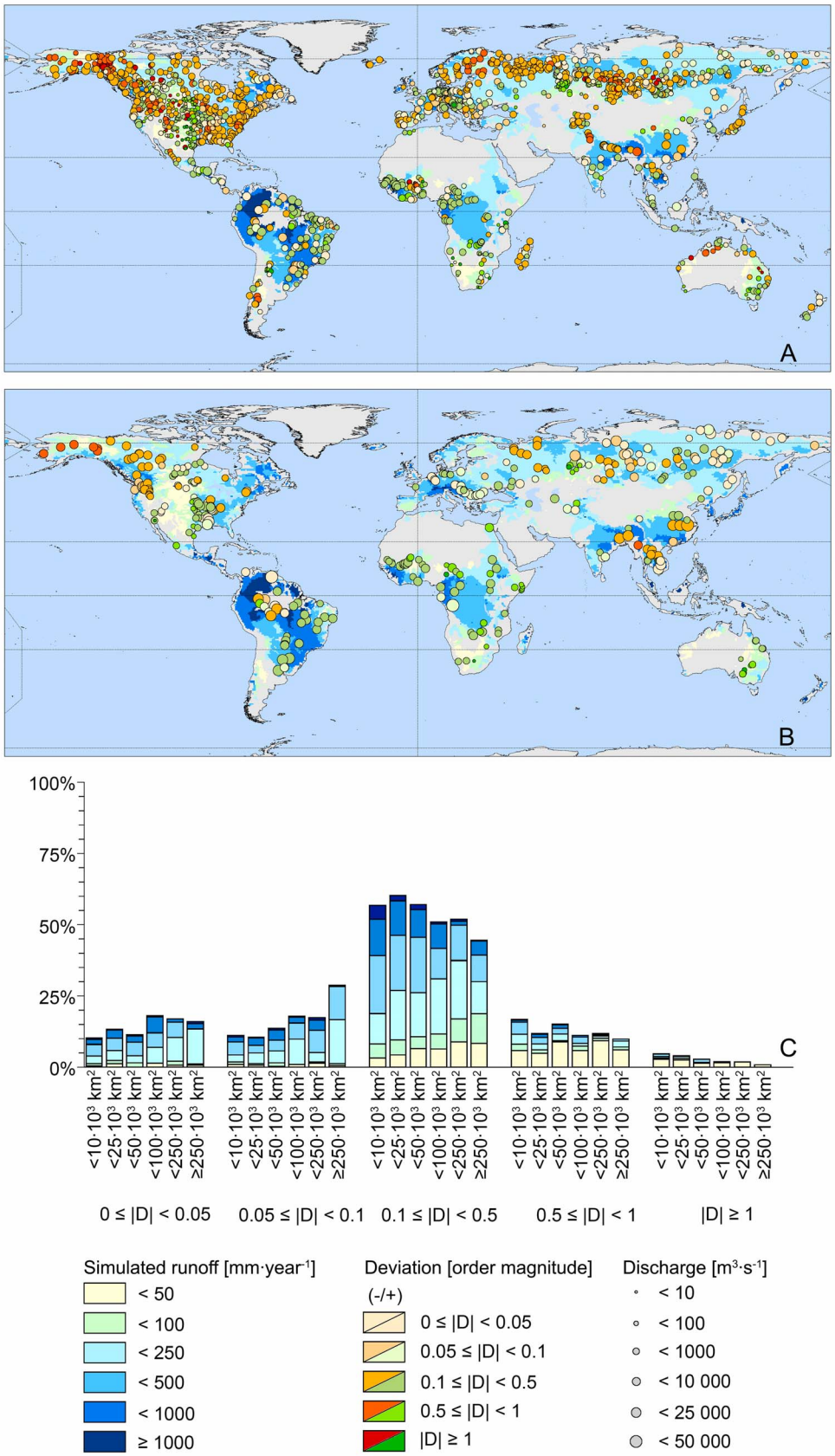

Figure 5. Deviations, D (dimensionless), in catchment-averaged runoff depth. Deviations are expressed in terms of order of magnitude (dimensionless) for 1938 long-term GRDC stations: (a) small catchments (<100,000 km^2), (b) large catchments (≥100,000 km^2), and (c) global summary where values stack to 100% per class of catchment area. The background color in Figures 5a and 5b is the simulated runoff.

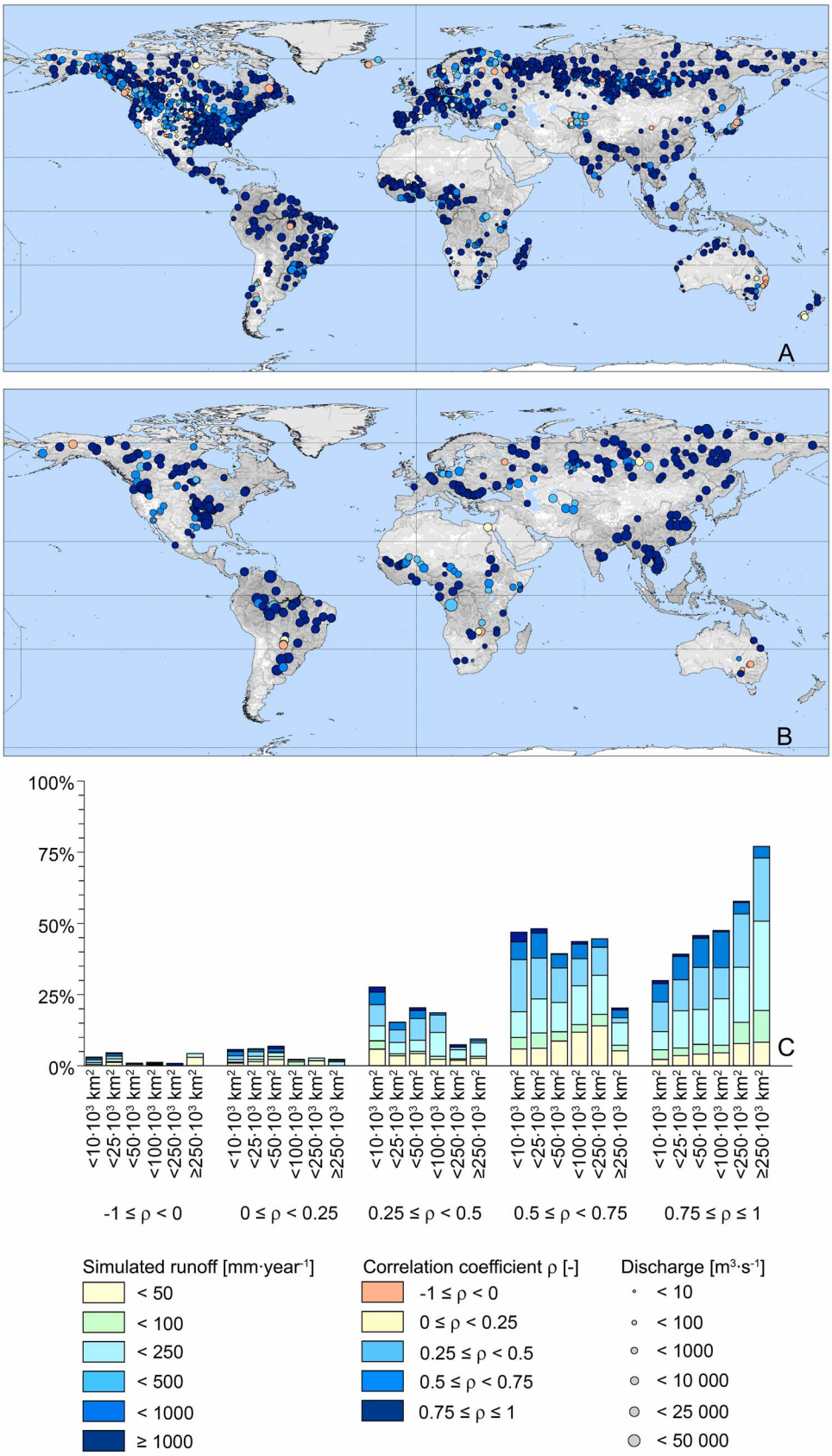

Figure 6. Correlation coefficient, ρ (dimensionless), for the climatology of monthly discharge for 1938 long-term GRDC stations: (a) small catchments (<100,000 km^2), (b) large catchments (≥100,000 km^2), and (c) global summary where values stack to 100% per class of catchment area. The background color in Figures 6a and 6b is the simulated discharge.

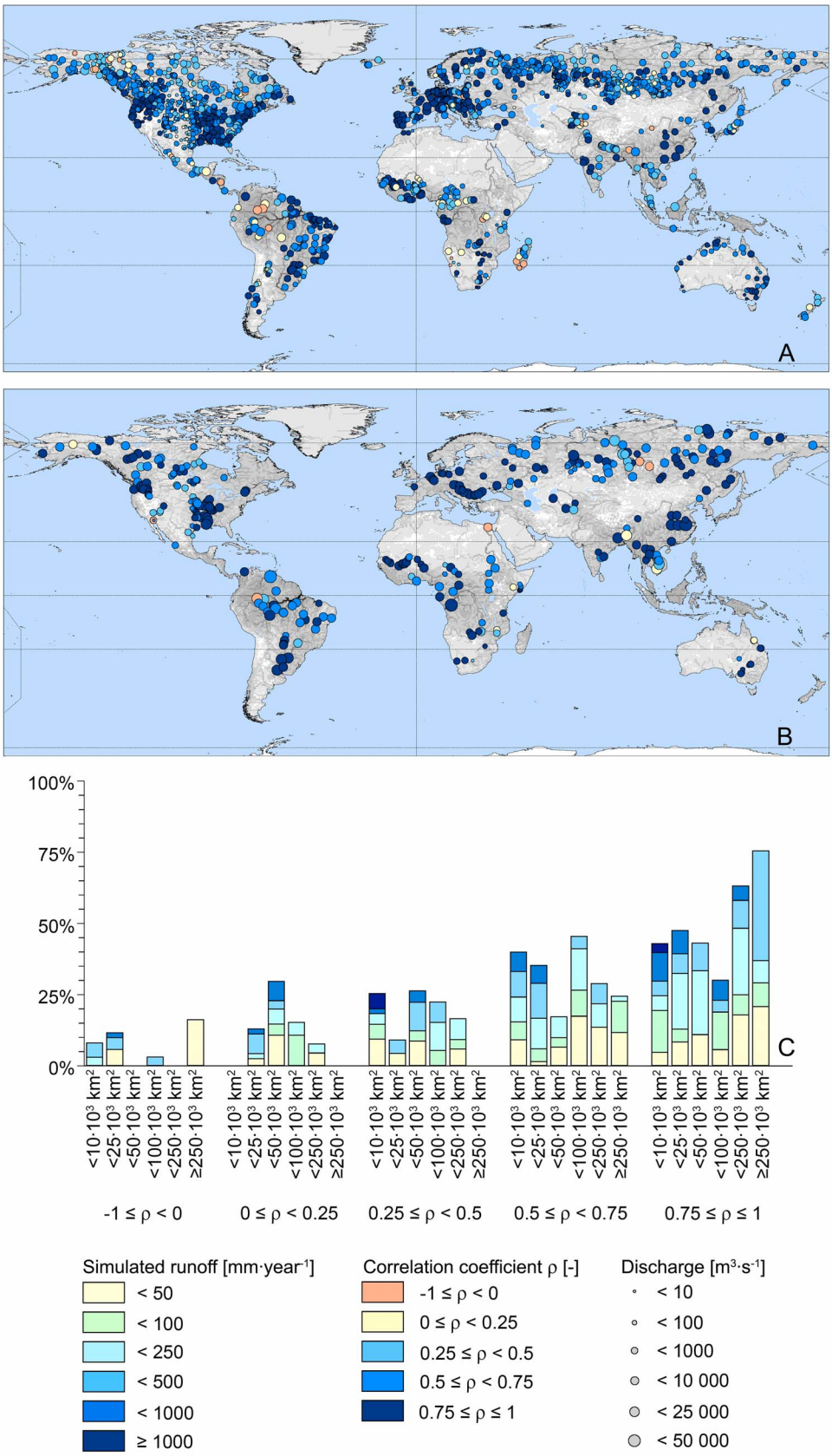

Figure 7. Correlation coefficient, ρ (dimensionless), for the time series of annual discharge for 1938 long-term GRDC stations: (a) small catchments (<100,000 km^2), (b) large catchments (≥100,000 km^2), and (c) global summary where values stack to 100% per class of catchment area. The background color in Figures 7a and 7b is the simulated discharge.

Table 3. Model Performance on a Monthly Basis for the Selection of Large River Basins[a]

River	N	α	R^2
Amazon	334	1.22	0.95
Orinoco	384	0.98	0.92
Parana	406	0.71 (0.65)	0.93 (0.89)
Congo	312	0.80	0.95
Nile	144	0.15 (0.12)	0.85 (0.82)
Blue Nile	300	0.56 (0.53)	0.75 (0.80)
White Nile	456	0.20 (0.21)	0.90 (0.92)
Niger	405	0.20	0.54
Orange	242	0.23 (0.20)	0.53 (0.54)
Zambezi	447	0.47	0.75
Murray	525	0.26 (0.20)	0.57 (0.60)
Mekong	432	1.35 (1.32)	0.92 (0.92)
Brahmaputra	154	1.46 (1.45)	0.96 (0.96)
Ganges	190	1.07 (0.97)	0.94 (0.94)
Indus	126	0.78 (0.66)	0.54 (0.62)
Yangtze	372	1.32 (1.31)	0.97 (0.98)
Huang He	372	0.74 (0.61)	0.64 (0.91)
Mississippi	501	1.24 (1.10)	0.94 (0.93)
Columbia	501	1.38 (1.27)	0.85 (0.94)
Mackenzie	415	1.63 (1.65)	0.88 (0.88)
Lena	528	1.22 (1.21)	0.75 (0.77)
Volga	492	1.19 (0.96)	0.70 (0.82)
Dniepr	324	0.77 (0.70)	0.76 (0.90)
Danube	516	0.90 (0.85)	0.97 (0.97)
Rhine	528	1.03 (0.98)	0.96 (0.96)
Elbe	525	0.70 (0.66)	0.84 (0.84)

[a]Slope, α (dimensionless), and coefficient of determination, R^2 (dimensionless), are calculated from the regression of the observed on the simulated monthly discharge with the intercept forced through the origin. N represents the number of months with observed discharge during the simulation period (1958–2001). Where modified discharge, because of the presence of reservoirs or water demand, does not have perceptible influence on the outcome, the given value is based on the natural discharge; where two values are given, the first value pertains to the modified discharge, while the one given in parentheses pertains to the natural discharge.

indicate how well the temporal variation in streamflow is approximated over the season and over a period of multiple years. Correlation was preferred over the Nash-Sutcliffe model efficiency in case of the long-term statistics as the latter is severely influenced by any deviation in mean discharge and by the limited number of observations that might be available. In total, a subset of 1938 stations had all information available to calculate these statistics. Similarly, temporal performance was investigated for the 26 selected stations through the slope, α, and the coefficient of determination, R^2 (Tables 3 and 4). The observed and simulated regime curves for these basins and selected hydrographs are shown in Figures 8a and 9. For these selected 26 stations, the simulated natural discharge and the modified discharge are shown as the difference between these regimes is the largest (e.g., Figure 4b).

3.1.3. Long-Term Statistics of Discharge and Runoff

[33] Regulation by reservoirs has little effect on the long-term mean annual discharge (Figure 3). Downstream decreases arise from the increased evaporation over the variable reservoir areas (e.g., Volga, Nile) while some water may be gained from an increase in net precipitation (e.g., Churchill, Fraser). Locally, the introduction of reservoirs leads to a reclassification of cells from rivers to reservoirs and changes in the drainage network as streams are diverted to a single outlet (e.g., for the upper Missouri River). Since the reservoir release is assigned to the entire reservoir whereas downstream cells are starved from inflow, this introduces some relatively large deviations from the conditions of natural discharge. However, total streamflow volumes are hardly affected. In contrast, considering water demand by means of the modified discharge leads to a decrease which is prominent for the rivers crossing major irrigated areas of the world, including the upper course of the Mississippi, Amur Darya, Indus, Huang He, and Murray-Darling.

[34] Because of the large number of catchments without reservoirs and variations in water demand, the regression analysis shows little variation in performance when either natural discharge, regulated discharge or modified discharge are considered and thus only the results for the natural discharge are presented in the subsequent analyses. The statistics calculated from observations over the actual simulation period are slightly better than those calculated over all available observations (Table 5). In all instances, the coefficient of determination (R^2) is high but the coefficient of determination decreases when the mean minimum and maximum monthly discharge or the mean runoff are considered instead of the mean discharge. In terms of slope, there is little variation between the mean discharge and the runoff and values are just below unity (Figure 4). This suggests that on average the runoff depth and the accumulated discharge can be reasonably approximated by the model although they are on average overestimated. For the

Table 4. Model Performance on an Annual Basis for the Selection of Large River Basins[a]

River	N	α	R^2
Amazon	26	1.26	0.99
Orinoco	32	0.99	0.99
Parana	33	0.74 (0.73)	0.90 (0.98)
Congo	26	0.82	1.00
Nile	12	0.16 (0.14)	0.98 (0.98)
Blue Nile	25	0.43 (0.42)	0.97 (0.97)
White Nile	38	0.21 (0.22)	0.98 (0.98)
Niger	33	0.30	0.97
Orange	9	0.27 (0.22)	0.82 (0.78)
Zambezi	37	0.60	0.95
Murray	43	0.28 (0.20)	0.83 (0.80)
Mekong	36	1.33 (1.31)	0.99 (0.99)
Brahmaputra	11	1.54 (1.52)	0.99 (0.99)
Ganges	13	1.07 (0.92)	0.99 (0.99)
Indus	8	0.70 (0.56)	0.96 (0.97)
Yangtze	31	1.28 (1.28)	1.00 (1.00)
Huang He	31	0.86 (0.62)	0.98 (0.98)
Mississippi	41	1.23 (1.11)	1.00 (1.00)
Columbia	41	1.42 (1.32)	0.99 (0.99)
Mackenzie	28	1.45 (1.47)	0.99 (1.00)
Lena	44	1.00 (0.99)	1.00 (1.00)
Volga	41	1.30 (1.06)	0.97 (0.99)
Dniepr	27	0.87 (0.72)	0.97 (0.98)
Danube	43	0.91 (0.85)	1.00 (1.00)
Rhine	44	1.04 (0.98)	1.00 (1.00)
Elbe	43	0.75 (0.69)	0.98 (0.98)

[a]Slope, α (dimensionless), and coefficient of determination, R^2 (dimensionless), are calculated from the regression of the observed on the simulated monthly discharge with the intercept forced through the origin. N represents the number of months with observed discharge during the simulation period (1958–2001). Where modified discharge, because of the presence of reservoirs or water demand, does not have perceptible influence on the outcome, the given value is based on the natural discharge; where two values are given, the first value pertains to the modified discharge, while the one given in parentheses pertains to the natural discharge.

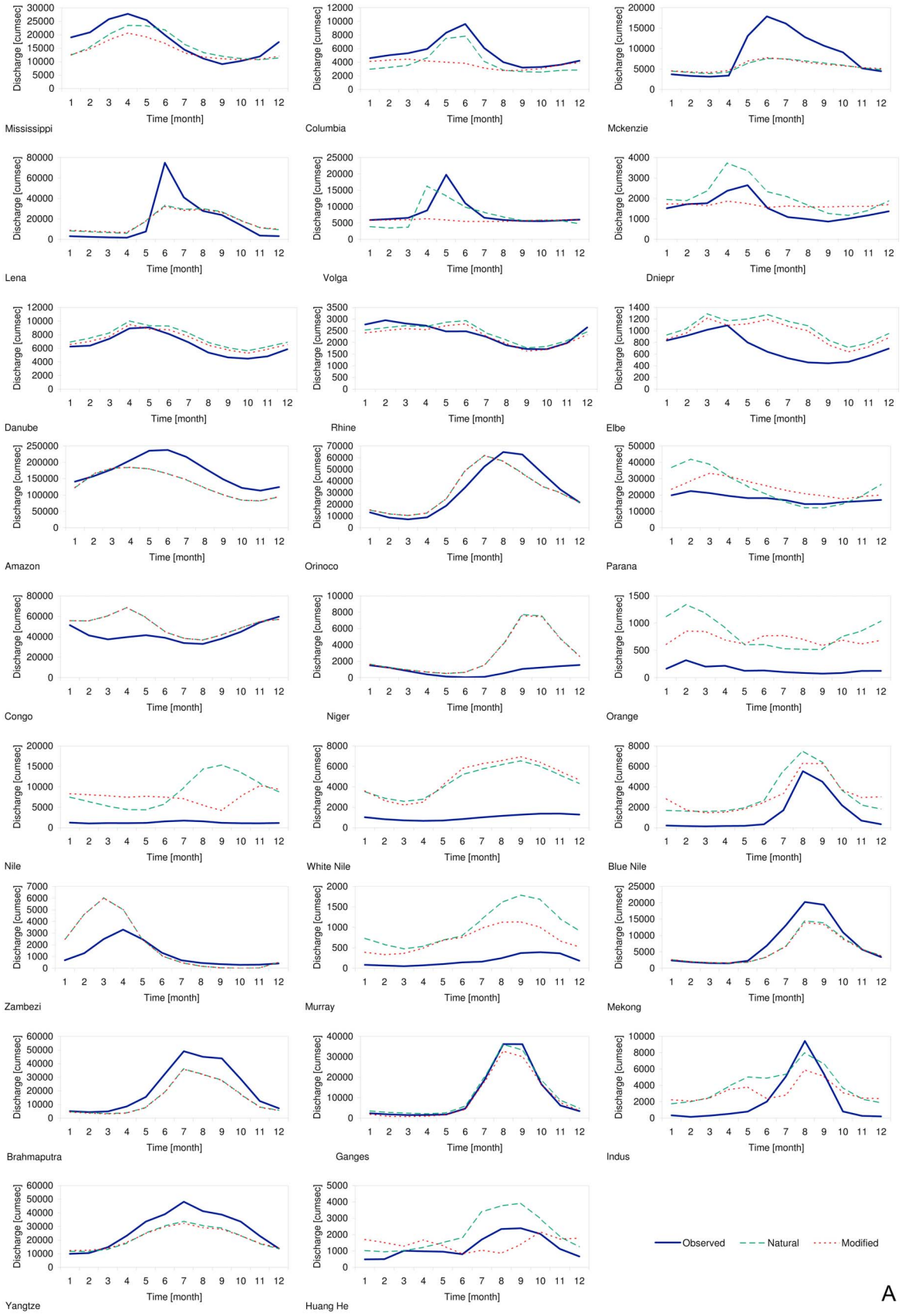

Figure 8. Regime curves of mean monthly discharge for (a) the selected GRDC stations on large rivers and (b) a number of reservoirs. For the reservoir of the High Aswan Dam, the gray dashed line represents the actual reservoir release when scaled to the mean of the simulated release.

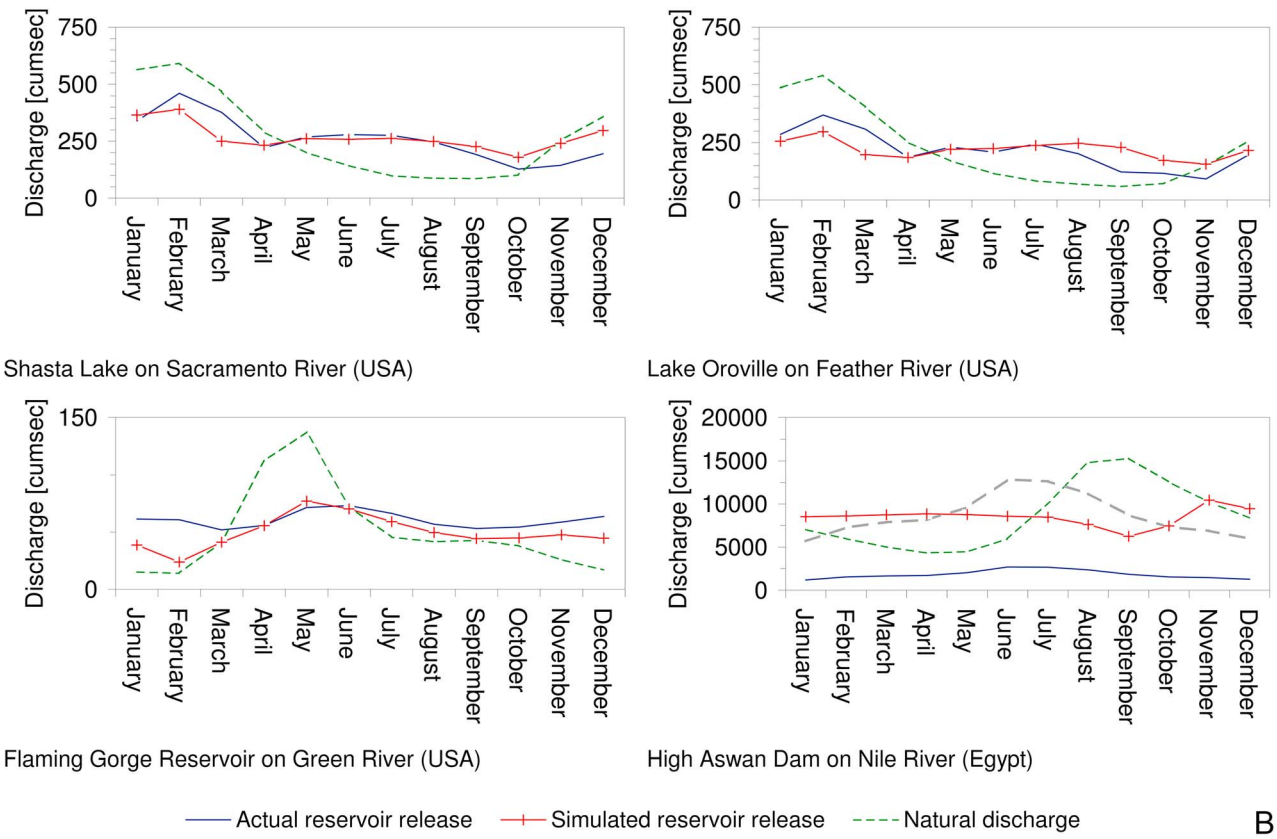

Figure 8. (continued)

extreme discharges, the effect of overestimation is clearer in case of the minimum monthly discharge while less variability can be explained in case of the maximum monthly value. Looking at the average discharge, the spread around the 1:1 line decreases when the basin area increases and more runoff is accumulated (Figure 4a). Still, the tendency of the model to overestimate the discharge can also be recognized in Figure 4b, but the data points center more on the 1:1 line, especially for the larger basins and when the modified discharge is considered. When expressed as runoff, the slope lies closer to unity but the spread remains large (Table 5 and Figure 4c). When evaluating the deviations in catchment-averaged runoff globally, zones of limited performance can be found (Figure 5). The apparent zones of limited performance for the larger catchments (>100,000 km^2) are also present when the smaller catchments are considered, albeit with some added noise and intensity. The first two categories with absolute deviations of 0.05 and 0.1 orders of magnitude represent in total 15.8 and 24.4% of the gauged catchment area of the long-term GRDC data set globally. These values correspond closely with the frequencies for the largest catchments (≥250 000 km^2) which means that performance is largely defined by a number of large catchments of good to adequate performance (based on totaled area over all subcategories). The category $0.1 \leq |R| < 0.5$ represents 47.6% of the gauged area, bringing the total of catchments for which the simulated and observed runoff deviate by less than half an order of magnitude to 88%. For the larger basins, the performance of the model in terms of runoff depth is good in case of the Congo, Orinoco, Volga and Rhine (less than 0.1 order of magnitude deviation; Figure 5b). Also, deviations at the mouth of large basins are generally small even where those at upstream stations are relatively large (e.g., Danube, Mississippi, Mekong and the Yenisei River). However, model performance decreases with decreasing catchment size and is the lowest for the drier catchments with less than 50 mm throughout (Figure 5c). Equally, runoff is generally underestimated in the arctic and subarctic regions, in particular for those of North America, large rivers like the Yukon and Mackenzie inclusive.

3.1.4. Seasonality

[35] In terms of temporal variability, the model performs well (Figures 6 and 7), although the model captures intra-annual variability or seasonality, as represented by the monthly climatology, better than the interannual variability (Figures 6c and 7c). In terms of seasonality, 75% of the gauged area has a correlation coefficient that is larger than 0.75 (area-weighted fraction over the last category of Figure 6c). Similar to the comparison of runoff depth, smaller catchments and those with less effective precipitation perform worse. If any trends are discernible, it seems that the observed seasonality is only moderately resolved by the model for the larger catchments along the Pacific cordilleras of North America, the Sahel and the adjacent parts of the Congo and Nile basins, for the endorheic basins of central Asia (e.g., the Amur Darya) and for the northern European rivers draining toward the Baltic Sea

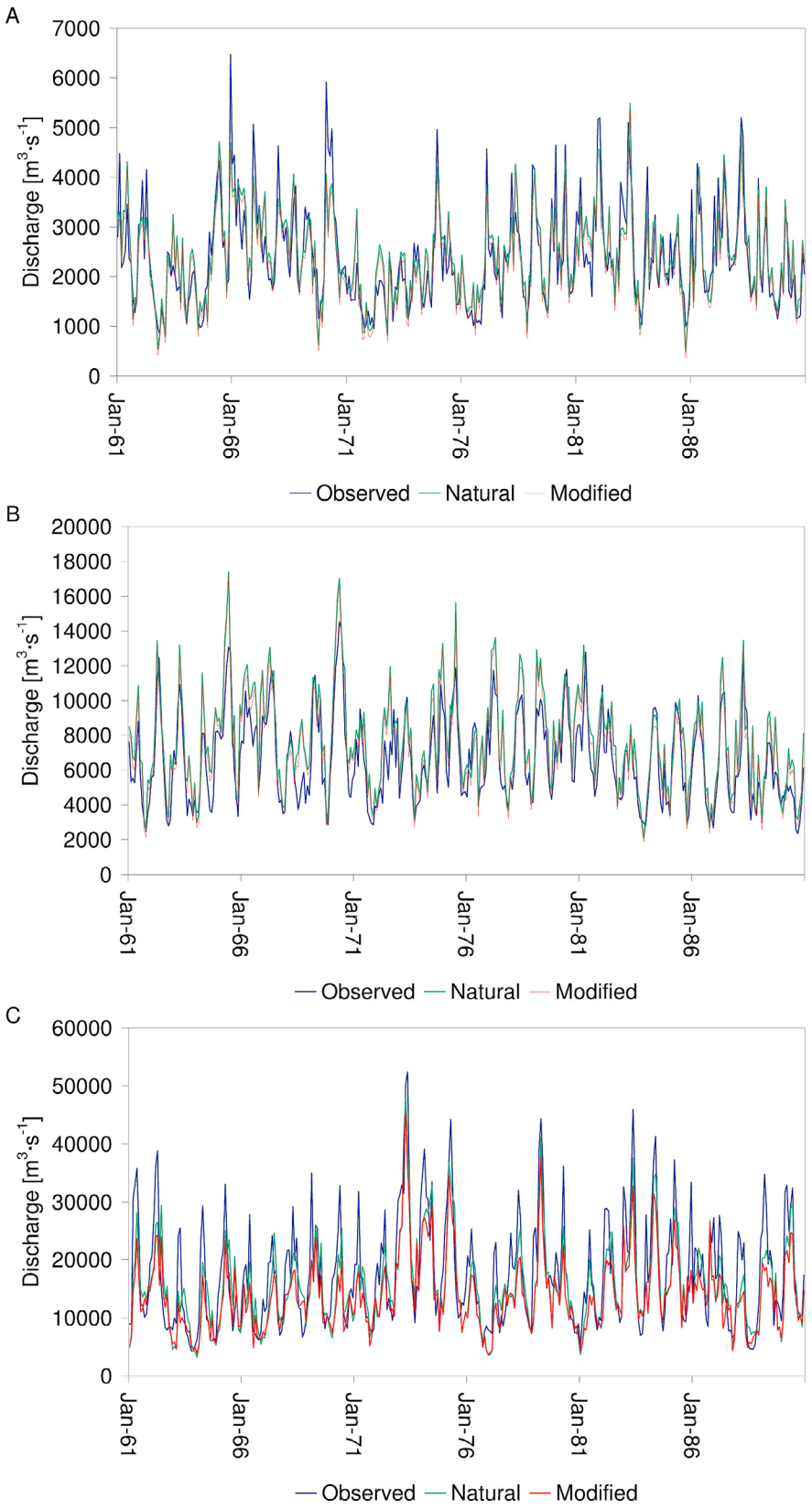

Figure 9. Hydrographs of monthly discharge over the period 1961–1990: (a) Rhine, (b) Danube, and (c) Mississippi.

Table 5. Regression Analysis on Descriptive Statistics From the Long-Term GRDC Data Set[a]

	Long-Term Statistic (N = 2219)		Simulation Period 1958–2001 (N = 1978)	
	α	R^2	α	R^2
Monthly discharge Q (m^3 s^{-1})				
Minimum	0.797	0.883	0.799	0.855
Mean	0.892	0.894	0.904	0.909
Maximum	0.865	0.743	0.916	0.775
Mean runoff R (mm yr^{-1})	0.981	0.761	0.985	0.766

[a]Slope, α (dimensionless), and coefficient of determination, R^2 (dimensionless), are calculated from the regression of the long-term statistics of observed discharge on those for the simulated natural streamflow with the intercept forced through the origin. Evaluated are all long-term statistics from the GRDC inventory [*GRDC*, 2008] and those for stations with matching data (10 years or more) over the simulation period 1958–2001.

and German Bight (e.g., the Elbe; Figure 5b; see also Figure 8a). Some stations perform poorly because of the presence of upstream reservoirs (e.g., Kafue and Nile in Africa, the station at the Rybinsk dam on the Volga, the stations on the Angara in Siberia and the stations in the Murray-Darling Basin).

[36] The effect of the reservoir scheme is visible in some of the regime curves of Figure 8b and in the performance statistics of Table 3. Reservoir operations influence the shape of the hydrograph (e.g., the Parana) as well as the volume under the curve (e.g., the Volga, see also Figure 3b); the former is a direct effect of the simulated release whereas the latter reflects changes in the gains and losses over the dynamic reservoir surface. In terms of performance, it should be noted that the inclusion of the reservoir scheme has often only a small effect on the seasonal performance. Some improvement is found for the Parana, Nile and Orange. In rivers with substantial water use and limited inflow (Indus, Murray), the natural discharge performs better than the regulated one although the inclusion of water demand in the latter in the form of modified discharge introduces an improvement in the slope and a marginal increase in the coefficient of determination (Table 3). Similarly, natural discharge performs better for regulated catchments were the main purpose is hydropower generation and flood control, for which the simulated regulated discharge becomes too constant over time (Huang He, Dnepr, Volga, and Columbia). Yet outside the peak flow season, the regulated discharge compares more favorably with the observed discharge, when the simulated natural discharge falls below the observed levels. Figure 8b also provides examples of simulated and observed releases for three reservoirs in the southwestern United States and the Aswan Dam (Egypt) for which the main purpose is water supply. Despite the limited performance of the hydrological model in the more arid regions of the world, the simulated regulated release follows the actual release closely for reservoirs in the southwestern United States. The simulated release is less satisfactory in case of the Aswan dam on the Nile. Besides the already signaled overestimation, actual release appears to be driven by a more seasonal demand than that considered by our model. In addition to the effects of simulated regulation, inspection of the regime curves and the performance statistics also shows there is often a shift in the timing of the average peak flow, despite the high coefficient of determination (Figure 6 and Table 3). This applies to tropical rivers, such as the Amazon, Orinoco, Zambezi and Congo, and to snowmelt dominated and influenced rivers such as the Lena, Mackenzie, Mississippi and Rhine. The seasonality of the monsoon-dominated rivers in Asia is generally well approximated despite differences in runoff depth (e.g., Mekong and Brahmaputra) with the exception of the Indus, where the runoff depths is overestimated and two discharge peaks are simulated rather than one as observed. Similarly, the performance is low for other catchments with limited rainfall and elevated water use such as the Orange, Murray, and Niger. The same is observed for the Nile although the performance of the monsoon-dominated Blue Nile in terms of volume and timing is slightly better. For all African rivers overestimation of the runoff depth already occurs in their headwaters and persists along their entire course.

3.1.5. Interannual Variability

[37] In terms of interannual variability, the picture is more varied. The model captures the interannual variability well although the performance is slightly below that of the seasonality; 60% of the gauged area still has a correlation coefficient larger than 0.75 (area-weighted total over the last category of Figure 6c). The tendency that performance increases with catchment size and effective precipitation, as observed for the runoff depth and seasonality, is not as strong in this case. In some cases (e.g., Nile, Brahmaputra, and Mekong), the performance decreases near the outlet of a basin, even though the interannual variability is simulated adequately upstream (Figures 7a and 7b). Since this comparison is based on the simulated natural discharge, some of the performance can be attributed to reservoir operations (e.g., the stations on the Angara in Siberia and the Fitzroy and Burdekin in northeast Australia; Figure 7b). This cannot explain all the deficiency in performance, however, as is the case for the station on the Yukon that performs poorly in terms of the monthly and interannual temporal variability (Figures 6b and 7b). For the larger basins, performance as expressed by the coefficient of determination remains consistently large (R^2 > 0.80; Table 4). Monthly hydrographs for the Rhine, Danube and Mississippi are shown in Figure 9 as examples of rivers with an excellent representation of interannual variability.

3.1.6. Continental Runoff

[38] The above analysis provides a detailed overview of the performance of the model for particular catchments. It is assumed that the observation error is small compared to that introduced by the model structure and its parameterization. Yet, in light of a global study on water availability, it is equally informative to evaluate performance in relation to observation and model-based estimates of runoff at the continental scale. Table 6 summarizes the estimated continental runoff volumes from different sources. On inspection, the model-based estimate is on average lower than the observation-based one for all continents and the world in total while the range of the model-based estimates is larger. The continental runoff volumes of PCR-GLOBWB differ slightly when reservoirs are included because of changes in the direct gains and losses over the variable reservoir areas and decreases for all continents when water demand is subtracted, particularly in the case of North America. Overall, our results correspond to the model-based runoff volumes per continent. Generally the values are slightly

Table 6. Estimates of Continental Runoff (in $km^3\ yr^{-1}$) Based on Observations and Simulations

	Continent							
	Europe	Asia	Africa	North America	South America	Oceania	Global[a]	Time Period
Data-based estimates								
Baumgartner and Reichel [1975]	2564	12,467	3409	5840	11,039	2394	37,713	-
Korzun et al. [1978]	2970	14,100	4600	8180	12,200	2510	44,560	-
L'vovich [1979]	3110	13,190	4225	5960	10,380	1965	38,830	-
Shiklomanov [1997]	2900	13,508	4040	7770	12,030	2400	42,648	1921–1990
Global Runoff Data Centre [2004]	3083	13,848	3690	6294	11,897	1722	40,533	1961–1990
Average	2925	13,423	3993	6809	11,509	2198	40,857	-
Model-based estimates								
Fekete et al. [2000]	2772	13,091	4517	5892	11,715	1320	39,319	-
Vörösmarty et al. [2000]	2770	13,700	4520	5890	11,700	714	39,294	1961–1990
Nijssen et al. [2001]	-	-	3615	6223	10,180	1712	36,006	1980–1993
Oki et al. [2001]	2191	9385	3616	3824	8789	1680	29,485	1987–1988
Döll et al. [2003]	2763	11,234	3592	5540	11,382	2239	36,687	1961–1990
Widén-Nilsson et al. [2007]	3669	13,611	3738	7009	9448	1129	38,605	1961–1990
Average	2833	12,204	3933	5730	10,536	1466	36,566	-
PCR-GLOBWB								
Natural	2585	11,659	4257	5617	10,583	2111	36,812	1958–2001
Regulated	2576	11,520	4175	5507	10,625	2098	36,501	1958–2001
Modified	2433	11,017	4095	5209	10,571	2062	35,387	1958–2001

[a]Excluding Antarctica.

lower, with the exception of Africa and Oceania, for which our estimates are above average. For Oceania, this value is close to the observation-based estimate, for Africa it is at the upper end of the observed and simulated ranges. The results of PCR-GLOBWB are most similar to the model results of *Döll et al.* [2003], with the exception of Africa and South America, where they are more similar to the results of *Fekete et al.* [2000] and *Nijssen et al.* [2001], respectively.

3.2. Comparison of Actual Evapotranspiration

[39] Green water availability helps to determine the amount of blue water needed for irrigation to meet the atmospheric demand over irrigated areas. Green water equals the actual evapotranspiration and its correct assessment is determined by the ability of the model to reduce the potential evapotranspiration under water limited conditions correctly. To some extent this ability is reflected by the performance to simulate runoff depths (see above). In order to evaluate this aspect of our simulations directly, the simulated actual evapotranspiration is compared with that from the ERA-40 reanalysis. Although the latter does not strictly speaking constitute an observational data set and has a coarser resolution than PCR-GLOBWB, the ERA-40 reanalysis provides an independent estimate of the actual evapotranspiration and accounts indirectly for the observed latent heat fluxes by means of data assimilation of atmospheric observations [*Kållberg et al.*, 2005]. As such, it provides a proxy to evaluate the simulated actual evapotranspiration over the period 1958–2001, at a regional-to-continental scale at which no observations are available [*Ruiz-Barradas and Nigam*, 2006]. A global comparison is made in Figure 10, while a similar comparison is made on a monthly basis for a number of major irrigated areas in Figure 11. These areas comprise some of the most intensely irrigated areas as identified from the data set of *Portmann et al.* [2008], containing zones with irrigation fractions in excess of 10% and are compared with the zonal averages for the nonirrigated areas between 15°N and 30°N and 30°N–45°N, which encompass the aforementioned irrigated areas (Figure 10). Although the irrigated areas are not included in the parameterization of the underlying land surface scheme, the ERA-40 reanalysis [*Wipfler et al.*, 2009] will account implicitly for irrigation. The reason is that evapotranspiration will tend to decrease the temperature as energy is lost as latent heat [*Kalnay and Cai*, 2003]. Since in the reanalysis the atmospheric moisture budget is not closed [*Trenberth et al.*, 2007], updates of the assimilation scheme using screen temperature data may result in an actual evapotranspiration that is larger than the available moisture over irrigated areas. This additional latent heat loss is required to meet the observed temperatures which are lower than those originally simulated by the numerical weather prediction model. In contrast, the simulated actual evapotranspiration of PCR-GLOBWB includes these irrigated areas by means of the crop factor (section 2.2) but cannot surpass the available soil moisture as the actual irrigation gift is not modeled. Thus, it is expected that for irrigated areas the simulated actual evapotranspiration of PCR-GLOBWB will be consistently lower than that of the ERA-40 over the growing season. The difference between the actual evapotranspiration of the ERA-40 reanalysis and that of PCR-GLOBWB then is a proxy for the transpiration of applied water. In Figure 11 the net irrigation water demand of *Wada et al.* [2011, equation (5)] is taken to be equivalent to the applied water and included for comparison.

[40] The broad patterns in the mean annual actual evapotranspiration of Figure 10a are equally represented in the ERA-40 reanalysis and most differences are less than 0.25 m yr^{-1} (Figure 10b), although the simulated values show more spatial detail and a stronger zonation. Besides over large evaporative water surfaces (e.g., the Caspian Sea, Lake Chad and Lake Eyre in Australia), differences in actual evapotranspiration can partly be explained by differences in precipitation (Figure 10c). This is the case for western Amazonia, the Sahel, and northern Australia where the CRU TS 2.1 reports higher precipitation totals, for Alaska where because of undercatch the precipitation is underestimated (see also section 3.1.3) and for the Andes and Himalayas where the orographic influence on precipitation seems to be

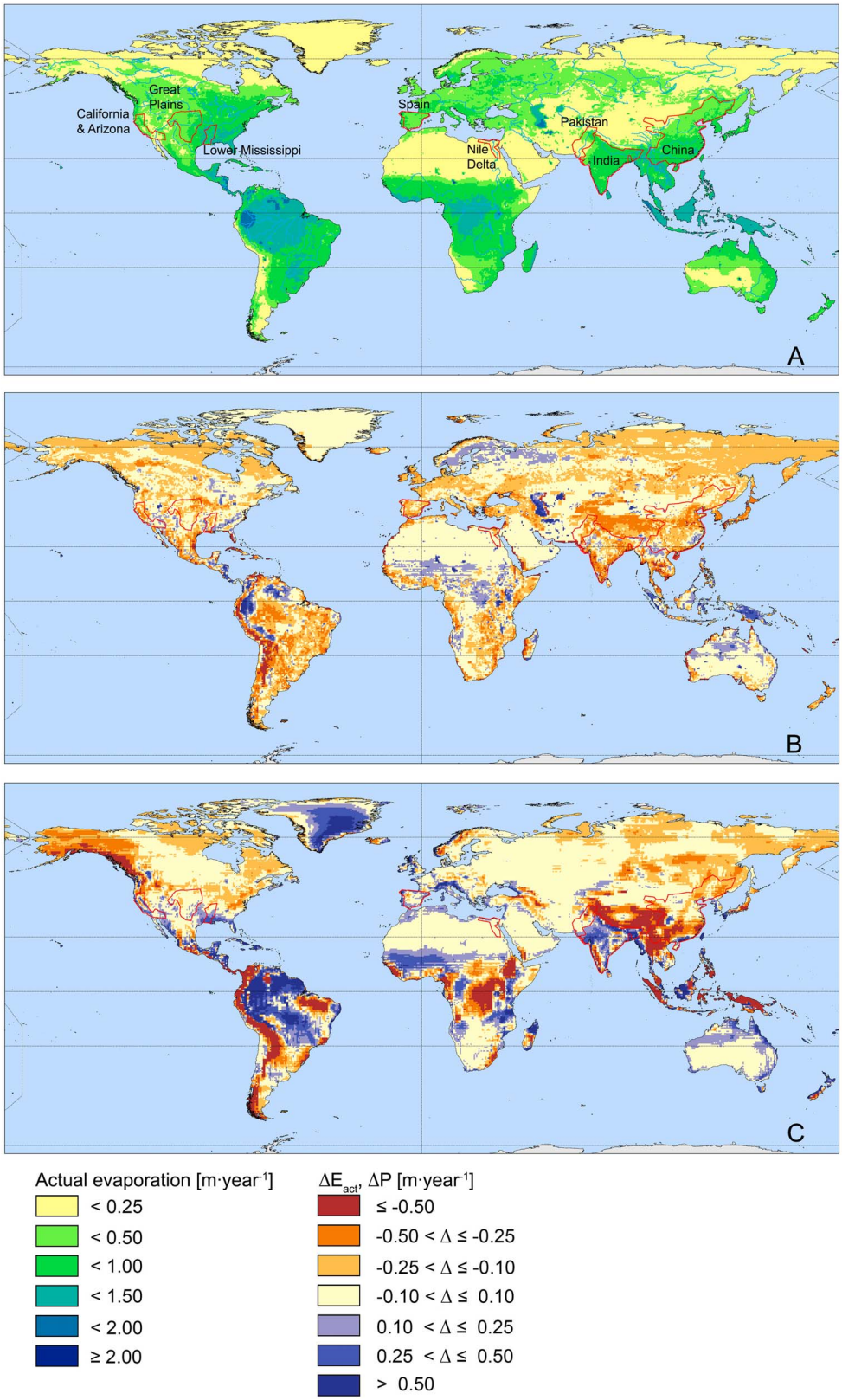

Figure 10. Comparison between actual evapotranspiration from PCR-GLOBWB and the ERA-40 reanalysis: Global fields: (a) mean annual actual evapotranspiration of PCR-GLOBWB (m yr^{-1}) with outline of major irrigated areas based on the work of *Portmann et al.* [2008] and the difference between the CRU-based forcing and the ERA-40 reanalysis for (b) mean annual actual evapotranspiration and (c) precipitation, both in m yr^{-1}. In Figures 10b and 10c, negative values (red) indicate that ERA-40 is larger; positive values (blue) indicate that CRU-based values are larger.

Figure 11. Comparison between actual evapotranspiration from PCR-GLOBWB and the ERA-40 reanalysis: (a) mean annual totals and (b) monthly values for major irrigated areas (see Figure 10 for locations).

underestimated by the CRU. Compared to the differences in precipitation, those in actual evapotranspiration are more subdued, as soil moisture availability reduces the rate at which water can be evaporated or transpired in the simulations. Evidently, this may remove some of the bias in the actual evapotranspiration but subsequently lead to larger biases in effective precipitation and discharge. Areas where evapotranspiration differs without any corresponding difference in precipitation are less frequent. Besides coastal regions with intricate shores (e.g., Norway) where the higher evaporation over the sea surface of the ERA-40 reanalysis bleeds onto the land surface, this concerns several tropical areas and the irrigated areas delineated in Figure 10a. Over the tropical areas, where water is not limiting, the simulated actual evapotranspiration is close to the potential rate and exceeds that of the ERA-40 (e.g., the Congo) while the precipitation rate is lower because of the positive bias in the precipitation over part of the simulation period in the ERA-40 reanalysis [*Troccoli and Kållberg*, 2004]. Similarly, ERA-40 precipitation is also higher over the nonirrigated areas for the zones between 15°N and 30°N and 30°N–45°N. This leads in turn to absolutely larger evapotranspiration values than simulated by PCR-GLOBWB although the difference becomes less marked as substantial parts of these areas are water limited.

[41] For most of the major irrigated areas, the simulated actual evapotranspiration is indeed smaller than that of the ERA-40 reanalysis while the overall rainfall is not very different (Figures 10b and 10c). This is shown in detail in the totals of Figure 11a which shows lower evaporation over the irrigated areas under the nonirrigated conditions of the simulation that define green water availability. Over the irrigated areas simulated actual evapotranspiration generally follows that of the ERA-40 reanalysis closely during the wet season but falls back during the dry season when the soil moisture deficit deepens (Figure 11b). This phenomenon is the strongest in areas where the growing season is shorter and one relies more on green water (e.g., California); where multiple crops are grown, this is less apparent (e.g., Pakistan). In these areas water is drawn more frequently from alternative sources or the demand may actually not be met as the totals and climatologies for the Nile Delta and Pakistan suggest (Figure 11). Including the net irrigation water demand brings the actual evapotranspiration rates of the simulation closer to those of the ERA-40 reanalysis, indicating that irrigation is likely to explain part of the difference.

4. Discussion and Conclusion

[42] In this first paper of a set of two on the temporal aspects of water stress on a global scale, we explored aspects of blue and green water availability in terms of river discharge and actual evapotranspiration by means of the macroscale hydrological model PCR-GLOBWB. This model was forced with the CRU TS 2.1 [*New et al.*, 1999, 2000], providing precipitation and air temperature directly and reference potential evapotranspiration indirectly through the FAO guidelines of *Allen et al.* [1998]. These monthly fields were broken down into daily data using the ERA-40 reanalysis [*Kållberg et al.*, 2005]. As such any errors in the ERA-40 reanalysis are overprinted by the CRU TS 2.1 data set that is based on observations. The CRU TS 2.1 compares well with other historical meteorological data sets [*Beck et al.*, 2004] but it is prone to uncertainties that are introduced by spatiotemporal variations in station density [*Hulme and New*, 1997]. The CRU TS 2.1 data set attempts to incorporate orographic effects by giving additional weight to elevation during interpolation and includes a large number of stations over the relevant period. Notwithstanding, there are regions where stations are sparse (e.g., Alaska), altogether absent (e.g., Congo Basin) or having highly variable densities (e.g., Amazonia) [*New et al.*, 2000] and these variations have repercussions on the ability of the CRU TS 2.1 to represent the climate over the period 1958–2001. As such it suffers from uncertainty in precipitation amounts and seasonality in the more arid regions [*Fekete et al.*, 2004] and, in combination with the problem of undercatch of snow [*Fiedler and Döll*, 2007] and elevation [*Briggs and Cogley*, 1996; *Adam et al.*, 2006], from uncertainty in precipitation amounts over the arctic and mountainous areas of the world. This uncertainty largely explains the bias in the catchment-averaged runoff depth of Figure 5 and the observed spread in Figure 4c. Its effect is pregnant for the Nile where the overestimation of runoff persists from its headwaters in the ITCZ to the station farthest downstream (Figure 5). It equally explains the better performance over those areas with dense observational networks such as Europe and large parts of North America.

[43] Hydrological model error is largely obscured by the precipitation bias, yet it is manifest for the drier regions of the world where runoff is consistently overestimated. Model errors in these areas concern the runoff generating mechanisms that are extremely difficult to capture [e.g., *Döll et al.*, 2003] and the underestimation of losses due to evapotranspiration and reinfiltration or withdrawals or diversions along the river channel. This applies to the Nile, where the bias increases toward the mouth, partly as a result of water use, partly as a result of insufficient evaporation over the wetlands of the Sudd [*Mohamed et al.*, 2005] (Figure 5). Withdrawals and diversions may also affect performance for rivers in temperate regions such as the Danube, Mississippi and the Yellow River, although the overestimation for this latter basin is matched by an underestimation for the Yangtze (Figure 5b). Subtracting water demand as considered here in the form of simulated modified discharge does improve performance for those rivers where the meteorological forcing is good (Rhine, Dnepr, Danube; Figure 4b) but obviously cannot remediate the errors where the forcing is poor (e.g., Nile).

[44] Generally, performance in terms of runoff depth increases with catchment size. This is logical for a macroscale hydrological model that cannot reproduce the fine detail that governs runoff generation in the smaller catchments. Model errors are more salient when looking at the temporal performance of the model. Still, forcing errors explain the poor performance in terms of interannual variability compared to that on a seasonal scale for the tropical and monsoon-dominated rivers such as the Congo and Mekong to some extent; especially over Africa temporal variability is poorly constrained because of the absence of observations. Apparent errors in the timing of the discharge can be deduced from the regime curves of Figure 8. For the Amazon and the Orinoco, the peak flood occurs too early, for the Congo too late and does not reproduce the secondary peak in May. This can be attributed to the

constant floodplain extent and the consequent errors in the resistance that is experienced by the flood wave. A similar shift in the timing of the peak discharge for the Congo was also found by *Zaitchik et al.* [2010] which they attribute to the complexity of the bimodal runoff regime and the poor quality of the GRDC gauge data. For the arctic and snow-influenced temperate rivers the timing of the snowmelt is the main reason for temporal shifts in the regime curves. Possible errors include the use of a constant melt rate and threshold temperature in the snow module. Also, the neglect of temperature variations at the subgrid scale can cause a too rapid snowmelt in mountainous terrain and may explain the early peak for the Volga, Dnepr, Columbia and Indus. For temperate rivers as the Mississippi and the Rhine, snowmelt occurs slightly too late and in addition to the above reasons rain-on-snow events may be an additional explanation of this phenomenon. This error, although striking in the regime curves, has, however, little influence on the temporal performance given the close similarity between observed and simulated discharge (Tables 3 and 4 and Figure 9). For the arctic rivers as the Lena and Mackenzie the underestimation of the peak flow is related to the partitioning of the snowmelt into direct runoff and base flow. Although permafrost is included statically in the parameterization of the model, the dynamic effect of ground frost on the infiltration capacity is ignored. Errors in floodplain resistance have an additional but minor effect as the floodplain extent is taken to be constant and ice formation and breakup are ignored. The differences in regime amplitude that were observed for the Mississippi and the Elbe equally arise from errors in the partitioning of effective precipitation into direct runoff and base flow. Water transferred to the groundwater reservoir is beyond the reach of evaporation and may lead to an overestimation in discharge, as is the case for the Elbe.

[45] Inclusion of the reservoir operation scheme (section 2.4) mostly affects the temporal performance of the model. The main difference of this reservoir scheme is that it is prospective rather than retrospective as the existing schemes of *Haddeland et al.* [2006] and *Hanasaki et al.* [2006]. It is directly implemented in the routing scheme and is updated by optimizing the monthly target storage per reservoir. To keep it tractable at the global scale reservoir release has been parameterized through the operational year of *Hanasaki et al.* [2006] and the amplitude of the release function of equation (12). On a daily basis it responds dynamically to changes in downstream demand and inflow, including that of upstream reservoirs. In combination with a constant price function, this choice leads to decreased performance for hydroelectric plants. For reservoirs with the main purpose of water supply, performance is generally much better (see also Figure 9) although it is ultimately controlled by the ability of the model to simulate the discharge well as the example for the High Aswan Dam illustrates. Such accumulated model error and the relatively simple rules of the reservoir operation scheme limit the performance of the model on a monthly scale (Table 3). In combination with short observation records (e.g., Nile; Table 3), dam completion may have an additional negative influence on the validation results of the regulated discharge as at least 52% of the dams was completed after 1970. Still, the reservoir operation scheme leads to a marginal better performance on an interannual scale as reservoirs ensure more persistent and secure flows (Table 4).

[46] Patterns of green water availability, expressed through the simulated actual evapotranspiration, are generally corroborated when that of the ERA-40 reanalysis is used as proxy (Figure 10), especially when the coarser resolution of the ERA-40 data set and differences in land surface parameterization are taken into account. For the major irrigated areas (Figure 11), the higher values of the updated actual evapotranspiration from the ERA-40 reanalysis in comparison to the simulated values over the growing season suggests that irrigation over these areas is significant and met from other sources than soil moisture. For temperate regions, the close similarity at the start of the growing season reveals the importance of green water as cultivation follows the wetter winter season (e.g., Spain). In areas where multiple crops can be harvested, the ERA-40 actual evapotranspiration is consistently larger and corresponds to the river-fed systems of the Indus and Nile. In these areas, simulated evapotranspiration losses exceed the actual evapotranspiration of the ERA-40 reanalysis. This highlights the uncertainty that is associated with the irrigated areas and the use of a prescribed cropping calendar. But it also stresses that the net irrigation demand is a theoretical maximum which may not be satisfied. Taking this in consideration, green water availability increased with net irrigation water demand appears to correspond generally well with the actual evapotranspiration rates approximated by the ERA-40 reanalysis.

[47] Given the comparison between simulated discharge and observations and that between the simulated actual evapotranspiration and that of the ERA-40 reanalysis we conclude that the model results are of sufficient quality to quantify water availability at the monthly time scale over the period 1958–2001 on a continental to global scale. Structural weaknesses result from the meteorological forcing and some model errors concerning runoff generation and discharge routing. The use of another meteorological data set than the CRU TS 2.1 may give lower errors but also would result in a loss of temporal variability as no other climatology covers such a large period and allows for a possible extension toward the start of the 20th century. Calibration could enhance model performance but may overcompensate for the uncertainty in the underlying precipitation product [*Biemans et al.*, 2009] and subsequent regionalization will confound the signal over ungauged basins and impair the physical basis of the model. The included prognostic reservoir scheme provides a computationally effective means to assess the influence of regulated discharge on water availability and potentially its development over time. Although its inclusion does not always increase model performance and is sensitive to errors in the simulated runoff, it is deemed to be an asset in this analysis as it allows quantifying the more persistent and securing flows as a result of the many reservoirs constructed during the period of interest. Therefore, we accept the underlying weaknesses, especially as they concern areas least susceptible to water scarcity such as sparsely populated and irrigated tropical and arctic regions or are directly related to water use, which is evaluated through water demand in the companion paper [*Wada et al.*, 2011].

[48] **Acknowledgments.** We are grateful to all the contributors of the many data sets that gave us the possibility to complete this study. In particular, we want to cordially thank Felix Portmann and Stefan Siebert of the Hydrology Group of Petra Döll, Institute of Physical Geography, Johann Wolfgang Goethe University (Frankfurt) for sharing the MIRCA2000 data

set with us. We also want to thank the anonymous reviewers and associate editor, whose comments on an earlier version of this set of papers contributed greatly to their present form and content. Y.W. is financially supported by Utrecht University Focus Areas Theme "Earth and Sustainability" (Project FM0906: Global Assessment of Water Resources).

References

Adam, J. C., E. A. Clark, and D. P. Lettenmaier (2006), Correction of global precipitation products for orographic effects, *J. Clim.*, *19*, 15–38, doi:10.1175/JCLI3604.1.

Adam, J. C., I. Haddeland, F. Su, and D. P. Lettenmaier (2007), Simulation of reservoir influences on annual and seasonal streamflow changes for the Lena, Yenisei, and Ob rivers, *J. Geophys. Res.*, *112*, D24114, doi:10.1029/2007JD008525.

Allen, R. G., L. S. Pereira, D. Raes, and M. Smith (1998), Crop evapotranspiration—Guidelines for computing crop water requirements, *Irrig. Drain. Pap. 56*, Food and Agric. Organ., Rome.

Avakyan, A. B., and S. P. Ovchinnikova (1971), Data on world reservoirs, *Power Technol. Eng.*, *5*, 773–777.

Baumgartner, A., and E. Reichel (1975), *The World Water Balance Mean Annual Global, Continental and Maritime Precipitation, Evaporation and Run-off*, Elsevier, Amsterdam.

Beck, C., J. Grieser, and B. Rudolf (2004), A new monthly precipitation climatology for the global land areas for the period 1951 to 2000, climate status report 2004, pp. 181–190, German Weather Serv., Offenbach.

Bergström, S. (1995), The HBV model, in *Computer Models of Watershed Hydrology*, edited by V. P. Singh, pp. 443–476, Water Resour. Publ., Highlands Ranch, Colo.

Biemans, H., R. W. A. Hutjes, P. Kabat, B. J. Strengers, D. Gerten, and S. Rost (2009), Effects of precipitation uncertainty on discharge calculations for main river basins, *J. Hydrometeorol.*, *10*, 1011–1025, doi:10.1175/2008JHM1067.1.

Biemans, H., I. Haddeland, P. Kabat, F. Ludwig, R. W. A. Hutjes, J. Heinke, W. von Bloh, and D. Gerten (2011), Impact of reservoirs on river discharge and irrigation water supply during the 20th century, *Water Resour. Res.*, *47*, W03509, doi:10.1029/2009WR008929.

Bos, M. G. (Ed.) (1989), *Discharge Measurement Structures*, 3rd rev. ed., Int. Inst. for Land Reclam. and Improv., Wageningen, Netherlands.

Briggs, P. R., and J. G. Cogley (1996), Topographic bias in mesoscale precipitation networks, *J. Clim.*, *9*, 205–218, doi:10.1175/1520-0442(1996)009<0205:TBIMPN>2.0.CO;2.

Chow, V. T., D. R. Maidment, and L. W. Mays (1988), *Applied Hydrology*, McGraw-Hill, New York.

Clapp, R. B., and G. M. Hornberger (1978), Empirical equations for some soil hydraulic properties, *Water Resour. Res.*, *14*, 601–604, doi:10.1029/WR014i004p00601.

Coe, M. T. (2000), Modeling terrestrial hydrological systems at the continental scale: Testing the accuracy of an atmospheric GCM, *J. Clim.*, *13*, 686–704, doi:10.1175/1520-0442(2000)013<0686:MTHSAT>2.0.CO;2.

Dingman, S. L. (1994), *Physical Hydrology*, Prentice-Hall, Upper Saddle River, N. J.

Döll, P., F. Kaspar, and B. Lehner (2003), A global hydrological model for deriving water availability indicators: Model tuning and validation, *J. Hydrol.*, *270*, 105–134, doi:10.1016/S0022-1694(02)00283-4.

Doorenbos, J., and W. O. Pruitt (1977), Crop water requirements, *Irrig. Drain. Pap. 24*, Food and Agric. Organ., Rome.

Dürr, H. H., M. Meybeck, and S. Dürr (2005), Lithologic composition of the Earth's continental surfaces derived from a new digital map emphasizing riverine material transfer, *Global Biogeochem. Cycles*, *19*, GB4S10, doi:10.1029/2005GB002515.

Dynesius, M., and C. Nilsson (1994), Fragmentation and flow regulation of river systems in the northern third of the world, *Science*, *266*, 753–762, doi:10.1126/science.266.5186.753.

Falkenmark, M. (1997), Meeting water requirements of an expanding world population, *Philos. Trans. R. Soc. London, Ser. B*, *352*, 929–936, doi:10.1098/rstb.1997.0072.

Fekete, B. M., C. J. Vörösmarty, and W. Grabs (2000), Global, composite runoff fields based on observed river discharge and simulated water balances, *Tech. Rep. 22*, Global Runoff Data Cent., Koblenz, Germany.

Fekete, B. M., C. J. Vörösmarty, J. O. Roads, and C. J. Willmott (2004), Uncertainties in precipitation and their impacts on runoff estimates, *J. Clim.*, *17*, 294–304, doi:10.1175/1520-0442(2004)017<0294:UIPATI>2.0.CO;2.

Fiedler, K., and P. Döll (2007), Global modelling continental water storage changes—Sensitivity to different climate data sets, *Adv. Geosci.*, *11*, 63–68, doi:10.5194/adgeo-11-63-2007.

Global Runoff Data Centre (GRDC) (2004), Long term mean annual freshwater surface water fluxes into the world oceans, comparisons of GRDC freshwater flux estimate with literature, Koblenz, Germany. [Available at http://grdc.bafg.de/servlet/is/7083/.]

Global Runoff Data Centre (GRDC) (2008), Long-term mean monthly discharges and annual characteristics of GRDC stations, report, Fed. Inst. of Hydrol., Koblenz, Germany.

Haddeland, I., T. Skaugen, and D. P. Lettenmaier (2006), Anthropogenic impacts on continental surface water fluxes, *Geophys. Res. Lett.*, *33*, L08406, doi:10.1029/2006GL026047.

Hagemann, S., and L. D. Gates (2003), Improving a sub-grid runoff parameterization scheme for climate models by the use of high resolution data derived from satellite observations, *Clim. Dyn.*, *21*, 349–359, doi:10.1007/s00382-003-0349-x.

Hagemann, S., M. Botzet, L. Dümenil, and B. Machenhauer (1999), Derivation of global GCM boundary conditions from 1 km land use satellite data, *Rep. 289*, Max Planck Inst. for Meteorol., Hamburg, Germany.

Hanasaki, N., S. Kanae, and T. Oki (2006), A reservoir operation scheme for global river routing models, *J. Hydrol.*, *327*, 22–41, doi:10.1016/j.jhydrol.2005.11.011.

Hulme, M., and M. New (1997), Dependence of large-scale precipitation climatologies on temporal and spatial sampling, *J. Clim.*, *10*, 1099–1113, doi:10.1175/1520-0442(1997)010<1099:DOLSPC>2.0.CO;2.

International Commission on Large Dams (ICOLD) (2003), *World Register of Dams: 1984 Full Edition and Update*, Paris.

Jackson, R. B., S. R. Carpenter, C. N. Dahm, D. M. McKnight, S. L. Postel, and S. W. Running (2001), Water in a changing world, *Ecol. Appl.*, *11*, 1027–1045, doi:10.1890/1051-0761(2001)011[1027:WIACW]2.0.CO;2.

Kållberg, P., P. Berrisford, B. Hoskins, A. Simmons, S. Uppala, S. Lamy-Thepaut, and R. Hine (2005), ERA-40 atlas, *ERA-40 Proj. Rep. Ser. 19*, Eur. Cent. for Medium Range Weather Forecasts, Reading, U. K.

Kalnay, E., and M. Cai (2003), Impact of urbanization and land-use change on climate, *Nature*, *423*, 528–531, doi:10.1038/nature01675.

Korzun, V. I., A. A. Sokolow, M. I. Budyko, K. P. Voskresensky, G. P. Kalininin, A. A. Konoplyanstev, E. S. Korotkevich, P. S. Kuzin, and M. I. Lvovich (Eds.) (1978), *World water balance and water resources of the Earth*, *Stud. Rep. Hydrol. 25*, U. N. Educ., Sci. and Cultural Organ., Paris.

Lehner, B., and P. Döll (2004), Development and validation of a global database of lakes, reservoirs and wetlands, *J. Hydrol.*, *296*, 1–22, doi:10.1016/j.jhydrol.2004.03.028.

Liebe, J., N. van de Giesen, and M. Andreini (2005), Estimation of small reservoir storage capacities in a semi-arid environment. Case study in the upper east region of Ghana, *Phys. Chem. Earth*, *30*, 448–454.

L'vovich, M. I. (1979), *World Water Resources and Their Future*, translated from Russian, AGU, Washington, D. C.

Meigh, J. R., A. A. McKenzie, and K. J. Sene (1999), A grid-based approach to water scarcity estimates for eastern and southern Africa, *Water Resour. Manage.*, *13*, 85–115, doi:10.1023/A:1008025703712.

Mitchell, T. D., and P. D. Jones (2005), An improved method of constructing a database of monthly climate observations and associated high-resolution grids, *Int. J. Climatol.*, *25*, 693–712, doi:10.1002/joc.1181.

Mohamed, Y. A., B. J. J. M. van den Hurk, H. H. G. Savenije, and W. G. M. Bastiaanssen (2005), Hydroclimatology of the Nile: Results from a regional climate model, *Hydrol. Earth Syst. Sci.*, *9*, 263–278, doi:10.5194/hess-9-263-2005.

Monteith, J. L. (1965), Evaporation and environment, *Symp. Soc. Exp. Biol.*, *19*, 205–224.

New, M., M. Hulme, and P. D. Jones (1999), Representing twentieth century space-time climate variability. Part 1: Development of a 1961–90 mean monthly terrestrial climatology, *J. Clim.*, *12*, 829–856, doi:10.1175/1520-0442(1999)012<0829:RTCSTC>2.0.CO;2.

New, M., M. Hulme, and P. D. Jones (2000), Representing twentieth century space-time climate variability. Part 2: Development of 1901–96 monthly grids of terrestrial surface climate, *J. Clim.*, *13*, 2217–2238, doi:10.1175/1520-0442(2000)013<2217:RTCSTC>2.0.CO;2.

Nijssen, B., G. M. O'Donnell, D. P. Lettenmaier, D. Lohmann, and E. F. Wood (2001), Predicting the discharge of global rivers, *J. Clim.*, *14*, 3307–3323, doi:10.1175/1520-0442(2001)014<3307:PTDOGR>2.0.CO;2.

Nilsson, C., C. A. Reidy, M. Dynesius, and C. Revenga (2005), Fragmentation and flow regulation of the world's large river systems, *Science*, *308*, 405–408, doi:10.1126/science.1107887.

Oki, T., and S. Kanae (2006), Global hydrological cycles and world water resources, *Science*, *313*, 1068–1072, doi:10.1126/science.1128845.

Oki, T., Y. Agata, S. Kanae, T. Saruhashi, D. Yang, and K. Musiake (2001), Global assessment of current water resources using total runoff-integrating pathways, *Hydrol. Sci. J.*, *46*, 983–995, doi:10.1080/02626660109492890.

Olson, J. S. (1994a), Global ecosystem framework—Definitions, internal report, Earth Resour. Observ. and Sci. Data Cent., U.S. Geol. Surv., Sioux Falls, S. D.

Olson, J. S. (1994b), Global ecosystem framework—Translation strategy, internal report, Earth Resour. Observ. and Sci. Data Cent., U.S. Geol. Surv., Sioux Falls, S. D.

Ormsbee, L. E., and A. Q. Khan (1989), A parametric model for steeply sloping forested watersheds, *Water Resour. Res.*, *20*, 1815–1822.

Portmann, F., S. Siebert, C. Bauer, and P. Döll (2008), Global data set of monthly growing areas of 26 irrigated crops, *Frankfurt Hydrol. Pap. 6*, Inst. of Phys. Geogr., Univ. of Frankfurt, Frankfurt am Main, Germany.

Postel, S. L., G. C. Daily, and P. R. Ehrlich (1996), Human appropriation of renewable fresh water, *Science*, *271*, 785–788, doi:10.1126/science.271.5250.785.

Rockström, J., M. Lannerstad, and M. Falkenmark (2007), Assessing the water challenge of a new green revolution in developing countries, *Proc. Natl. Acad. Sci. U. S. A.*, *104*, 6253–6260, doi:10.1073/pnas.0605739104.

Ruiz-Barradas, A., and S. Nigam (2006), Great Plains hydroclimate variability: The view from North American regional reanalysis, *J. Clim.*, *19*, 3004–3010, doi:10.1175/JCLI3768.1.

Shiklomanov, I. A. (Ed.) (1997), *Assessment of Water Resources and Water Availability in the World: Comprehensive Assessment of the Freshwater Resources of the World*, World Meteorol. Organ., Geneva, Switzerland.

Sloan, P. G., and I. D. Moore (1984), Modeling subsurface stormflow on steeply sloping forested watersheds, *Water Resour. Res.*, *20*, 1815–1822, doi:10.1029/WR020i012p01815.

Trenberth, K. E., L. Smith, T. Qian, A. Dai, and J. Fasullo (2007), Estimates of the global water budget and its annual cycle using observational and model data, *J. Hydrometeorol.*, *8*, 758–769, doi:10.1175/JHM600.1.

Troccoli, A., and P. Kållberg (2004), Precipitation correction in the ERA-40 reanalyses, *ERA-40 Proj. Rep. Ser. 13*, 6 pp., Eur. Cent. for Medium Range Weather Forecasts, Reading, U. K.

van Beek, L. P. H. (2008), Forcing PCR-GLOBWB with CRU meteorological data, report, Utrecht Univ., Utrecht, Netherlands. [Available at http://vanbeek.geo.uu.nl/suppinfo/vanbeek2008.pdf.]

van Beek, L. P. H., and M. F. P. Bierkens (2009), The global hydrological model PCR-GLOBWB: Conceptualization, parameterization and verification, report, Dep. of Phys. Geogr., Utrecht Univ., Utrecht, Netherlands. [Available at http://vanbeek.geo.uu.nl/suppinfo/vanbeekbierkens2009.pdf/.]

Verdin, K. L., and S. K. Greenlee (1996), Development of continental scale digital elevation models and extraction of hydrographic features, paper presented at 3rd International Conference/Workshop on Integrating GIS and Environmental Modeling, Natl. Cent. for Geogr. Inf. and Anal., Santa Barbara, Calif.

Vörösmarty, C. J., K. P. Sharma, B. M. Fekete, A. H. Copeland, J. Holden, J. Marble, and J. A. Lough (1997), The storage and aging of continental runoff in large reservoir systems of the world, *Ambio*, *26*, 210–219.

Vörösmarty, C. J., B. M. Fekete, and B. A. Tucker (1998), Global River Discharge, 1807–1991, Version 1.1 (RivDIS), http://daac.ornl.gov/RIVDIS/guides/rivdis_guide.html, Oak Ridge Natl. Lab. Distributed Arch. Cent., Oak Ridge, Tenn.

Vörösmarty, C. J., P. Green, J. Salisbury, and R. B. Lammers (2000), Global water resources: Vulnerability from climate change and population growth, *Science*, *289*, 284–288, doi:10.1126/science.289.5477.284.

Vörösmarty, C. J., et al. (2004), Humans transforming the global water system, *Eos Trans. AGU*, *85*(48), 509, doi:10.1029/2004EO480001.

Wada, Y., L. P. H. van Beek, D. Viviroli, H. H. Dürr, R. Weingartner, and M. F. P. Bierkens (2011), Global monthly water stress: 2. Water demand and severity of water stress, *Water Resour. Res.*, doi:10.1029/2010WR009792, in press.

Widén-Nilsson, E., S. Halldin, and C. Xu (2007), Global water-balance modelling with WASMOD-M: Parameter estimation and regionalization, *J. Hydrol.*, *340*, 105–118, doi:10.1016/j.jhydrol.2007.04.002.

Wipfler, E. L., K. Metselaar, J. C. van Dam, R. A. Feddes, E. van Meijgaard, L. H. van Ulft, B. van den Hurk, S. J. Zwart, and W. G. M. Bastiaanssen (2009), Seasonal evaluation of the land surface scheme HTESSEL against remote sensing derived energy fluxes of the Transdanubian region in Hungary, *Hydrol. Earth Syst. Sci. Discuss.*, *6*, 6293–6334, doi:10.5194/hessd-6-6293-2009.

Zaitchik, B. F., M. Rodell, and F. Olivera (2010), Evaluation of the global land data assimilation system using river discharge data and a source-to-sink routing scheme, *Water Resour. Res.*, *46*, W06507, doi:10.1029/2009WR007811.

M. F. P. Bierkens, L. P. H. van Beek, and Y. Wada, Department of Physical Geography, Utrecht University, Heidelberglaan 2, NL-3584 CS Utrecht, Netherlands. (r.vanbeek@geo.uu.nl)